Molecular Cell

Article

Condensed-phase signaling can expand kinase specificity and respond to macromolecular crowding

Graphical abstract

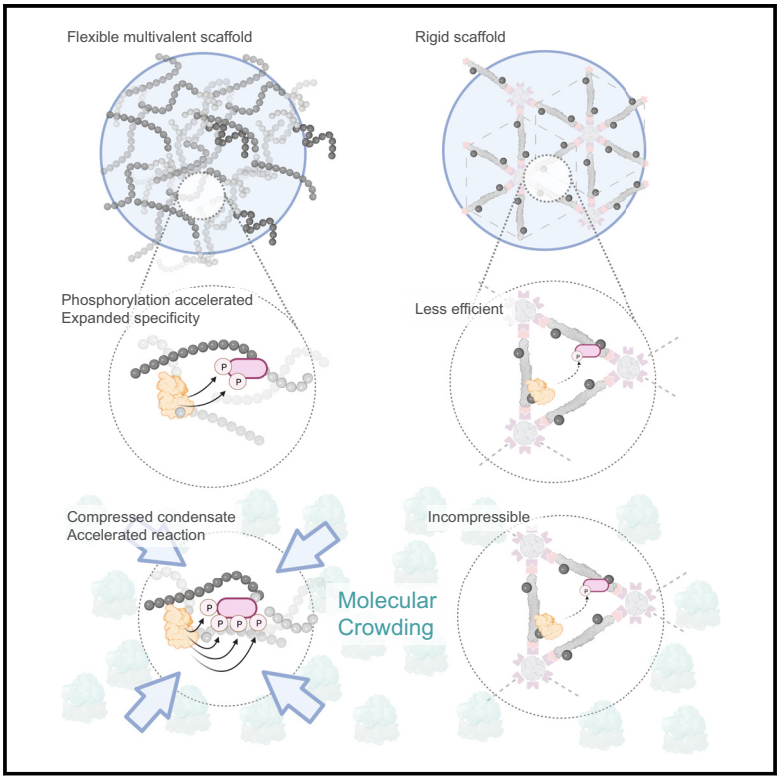

Authors

Dajun Sang, Tong Shu, Christian F. Pantoja, Alain Ibáñez de Opakua, Markus Zweckstetter, Liam J. Holt

Correspondence

mazw@mpinat.mpg.de (M.Z.), liam.holt@nyulangone.org (L.J.H.)

In brief

Sang et al. use synthetic biology to demonstrate that phase-separated biomolecular condensates can potentiate kinase signaling. Synthetic condensates allow the systematic exploration of features required for efficient signaling and responsiveness to biophysical cues. Finally, phase separation accelerates Alzheimer's-associated phosphorylation events.

Highlights

- Synthetic condensates enable the creation of dynamic phosphoregulation
- Kinases in condensates can phosphorylate unexpected peptides
- Kinases in condensates can convert biophysical information to chemical signals
- Alzheimer's-associated phosphorylation is accelerated by phase separation

Sang et al., 2022, Molecular Cell *82*, 3693–3711
October 6, 2022
https://doi.org/10.1016/j.molcel.2022.08.016

CellPress

Molecular Cell

CellPress
OPEN ACCESS

Article

Condensed-phase signaling can expand kinase specificity and respond to macromolecular crowding

Dajun Sang,[1] Tong Shu,[1] Christian F. Pantoja,[2] Alain Ibáñez de Opakua,[2] Markus Zweckstetter,[2,3,*] and Liam J. Holt[1,4,*]
[1]Institute for Systems Genetics, New York University Langone Medical Center, 435 E 30th Street, New York, NY 10010, USA
[2]German Center for Neurodegenerative Diseases (DZNE), Von-Siebold-Str. 3a, 37075 Göttingen, Germany
[3]Max Planck Institute for Multidisciplinary Sciences, Department of NMR-based Structural Biology, Am Fassberg 11, 37077 Göttingen, Germany
[4]Lead contact
*Correspondence: mazw@mpinat.mpg.de (M.Z.), liam.holt@nyulangone.org (L.J.H.)
https://doi.org/10.1016/j.molcel.2022.08.016

SUMMARY

Phase separation can concentrate biomolecules and accelerate reactions. However, the mechanisms and principles connecting this mesoscale organization to signaling dynamics are difficult to dissect because of the pleiotropic effects associated with disrupting endogenous condensates. To address this limitation, we engineered new phosphorylation reactions within synthetic condensates. We generally found increased activity and broadened kinase specificity. Phosphorylation dynamics within condensates were rapid and could drive cell-cycle-dependent localization changes. High client concentration within condensates was important but not the main factor for efficient phosphorylation. Rather, the availability of many excess client-binding sites together with a flexible scaffold was crucial. Phosphorylation within condensates was also modulated by changes in macromolecular crowding. Finally, the phosphorylation of the Alzheimer's-disease-associated protein Tau by cyclin-dependent kinase 2 was accelerated within condensates. Thus, condensates enable new signaling connections and can create sensors that respond to the biophysical properties of the cytoplasm.

INTRODUCTION

Eukaryotic cells use membrane bound organelles for spatiotemporal control of complex biochemical reactions, and there is increasing evidence for the importance of membraneless subcellular compartments, such as nucleoli or stress granules (Banani et al., 2017). These biomolecular condensates can be highly dynamic and sometimes form through liquid-liquid phase separation (LLPS) (Shin and Brangwynne, 2017). Recent research has revealed mechanisms of condensate formation, but it has been more difficult to demonstrate the importance of LLPS for the modulation of biochemical reactions.

It is difficult to understand the impact of condensation on biological regulation because mutations that disrupt LLPS or that perturb recruitment of clients to condensates can have pleiotropic effects. For example, although it is possible to mutate a protein sequence such that it fails to undergo LLPS, any associated loss of activity could be due to this loss of condensation or equally could be due to an unrelated loss of intrinsic protein function. A handful of studies have attempted to address this problem through orthogonal reconstitution of the condensation behavior. For example, chimeras of NELF condensates that recovered condensate formation and basic function but lost stress inducibility (Rawat et al., 2021). However, there are few examples, and they failed to fully rescue biological functions, illustrating our incomplete understanding of principles.

Synthetic biology is a powerful approach to investigate general principles while avoiding pleiotropic effects that can confound interpretation. For example, synthetic optogenetic systems, including "OptoDroplets" and "Corelets," were developed to exert spatiotemporal control of phase transitions in cells, permitting quantitative mapping of intracellular phase diagrams (Bracha et al., 2019; Shin et al., 2017).

The complex cellular environment can strongly affect LLPS. The cell interior is crowded, both in the cytosol and nucleus. Up to 40% of the cell volume is excluded by macromolecules (Delarue et al., 2018; Ellis and Minton, 2003; Luby-Phelps, 1999). Recent studies revealed that mTORC1 modulates cytoplasmic crowding by tuning ribosome concentration, and this has strong effects on phase separation (Delarue et al., 2018). In the nucleus, the chromatin network can mechanically suppress the coalescence of OptoDroplets, impacting condensate number, size, and placement (Lee et al., 2021; Zhang et al., 2021b). Since the crowded, active cell interior modulates phase

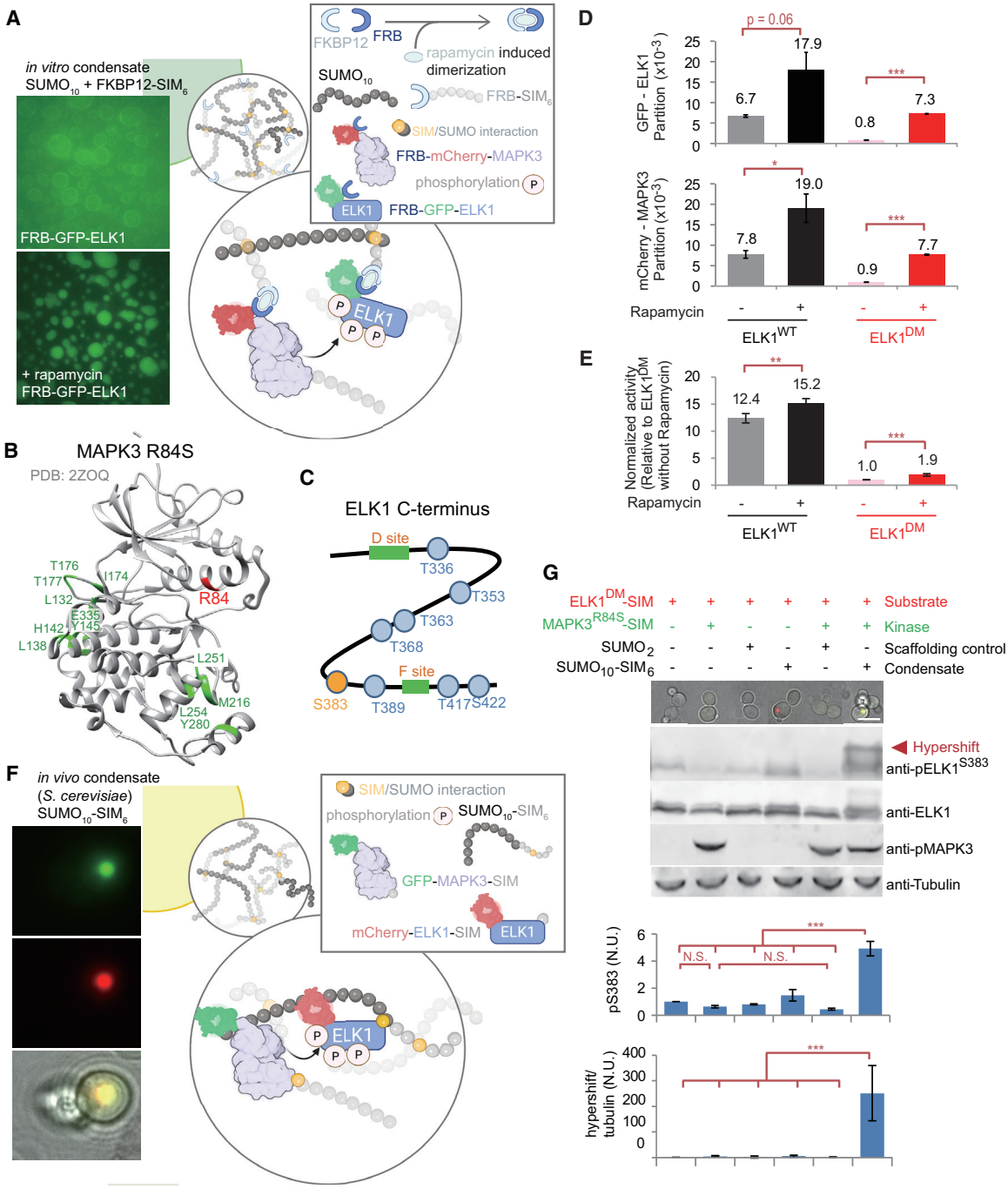

Figure 1. Recruitment into synthetic condensates increases phosphorylation rates

(A) Schematic of chemical dimerization approach. Mixture of $SUMO_{10}$ and SIM_6 leads to condensate formation. Rapamycin induces recruitment of MAPK3 (kinase) and ELK1 (substrate) into condensates.

(B) Structure MAPK3: R84 constitutive activation mutation, red; docking sites, green.

(C) Structure of the ELK1 C terminus. Blue circles are known phosphorylation sites targeted by MAPK3; phosphoepitope at S383, orange; docking motifs, green.

(D) ELK1 can be recruited to condensates. Total fraction of client that partitions into $SUMO_{10}$ + SIM_6 condensates ± rapamycin. n = 2.

(E) Recruitment to condensates increases phosphorylation *in vitro*. The C termini of ELK1 ($ELK1^{WT}$) or an ELK1 docking motif mutant ($ELK1^{DM}$) were used as substrates. n = 3.

(F) Schematic showing the approach to recruit clients into condensates in *S. cerevisiae*. $SUMO_{10}$-SIM_6 formed condensates. MAPK3 and ELK1 (clients) were tagged with SIM for recruitment into condensates.

(legend continued on next page)

separation, it follows that condensates should be capable of sensing crowding and transducing this information to chemical signals such as protein phosphorylation. However, there is little direct evidence of this biophysical sensing phenomenon.

Protein kinases regulate most aspects of eukaryotic cell biology. Kinase activity is strictly regulated, and kinases must discriminate between numerous proteins to find appropriate substrates. Defects in kinase activity regulation or loss of specificity can lead to human diseases such as cancer (Cicenas et al., 2018). Kinases exploit multiple mechanisms to achieve specificity, including subcellular localization, docking motif interactions, and recognition of consensus phosphorylation sites (Alexander et al., 2011; Howard et al., 2014; Mok et al., 2010; Reményi et al., 2006). For example, mitogen-associated protein kinases (MAP kinases) and cyclin-dependent kinase (CDK) family kinases prefer consensus phosphorylation motifs with a proline residue C-terminal to the phospho-acceptor site (Howard et al., 2014; Mok et al., 2010). Kinases can also use docking interactions for additional selectivity (Faustova et al., 2021; Howard et al., 2014; Miller and Turk, 2018; Örd and Loog, 2019; Örd et al., 2019). Several recent studies showed that a large number of kinases reside in condensates (Wippich et al., 2013; Zhang et al., 2021a), but it remains poorly understood how kinase activity is modified by recruitment to these structures. Therefore, it is of great interest to understand how kinase reaction specificity and activity can be affected within condensates.

Here, we use synthetic biology approaches to begin to uncover principles of condensed-phase signaling. We recruited the MAP kinases, MAPK3 and Fus3, and the cyclin-dependent kinase 1 (Cdk1) into multiple types of synthetic condensates formed of multivalent "scaffolds." We found that phosphorylation was increased by client recruitment into condensates both *in vitro* and *in vivo*. Kinase specificity was expanded in condensates, indicating that condensation can facilitate the creation of new links in phosphoregulatory networks. Substrates were phosphorylated in the absence of a docking motif and on non-consensus phospho-acceptor sequences. Phosphorylation within condensates could respond to dynamic changes in kinase activity within minutes. Systematic variation of scaffold and client properties revealed that beyond increasing client concentration (mass action), the availability of excess client-binding sites within the condensates and the flexibility of scaffolds strongly impacted reaction acceleration in condensates. We also found that phosphorylation within condensates can respond to molecular crowding, thus creating a biophysical sensor. Finally, we found that phosphorylation of the microtubule-binding protein, Tau, by cyclin-dependent kinase 2 (Cdk2) was accelerated in the condensed phase at sites associated with Alzheimer's disease, thus relating our insights from synthetic biology to possible new mechanisms for neurodegenerative disease.

RESULTS

Recruitment to synthetic condensates increases phosphorylation *in vitro*

Initially, we recruited a kinase and substrate to a synthetic condensate *in vitro*. The synthetic condensate was based on multivalent interactions between a tandem repeat of ten small ubiquitin-like modifier (SUMO) domains ($SUMO_{10}$) and a second polypeptide with six repeats of a SUMO Interacting Motif (SIM_6) (Figure 1A). $SUMO_{10}$ and SIM_6 readily undergo LLPS when mixed (Banani et al., 2016). Throughout this paper, we refer to proteins that form condensates as "scaffolds," proteins that are recruited to synthetic condensates as "clients."

The first clients we tested were the human Mitogen-Activated Protein kinase, MAPK3 (also called ERK1), and a C-terminal fragment of one of its substrates, ELK1. We took advantage of a constitutively active R84S mutant of MAPK3 (Figure 1B; Levin-Salomon et al., 2008) to simplify the system. The ELK1 C terminus contains multiple MAPK3 consensus phosphorylation motifs (Mylona et al., 2016) and two docking motifs (D site and F site) that bind to the surface of MAPK3. We tested the wild-type (WT) ELK1 C terminus (Figure 1C; residues 206–428, hereafter referred to as ELK1) and a version in which these two docking motifs were mutated (hereafter referred to as $ELK1^{DM}$; Figure S1A). To enable rapid recruitment of clients into condensates, we fused an FKBP12 domain to the N terminus of SIM_6 and an FRB domain and fluorescent protein (green fluorescent protein [GFP], or mCherry, for visualization) to the N terminus of each client. Dimerization of FKBP12 and FRB can be chemically induced by rapamycin. Initially, there was low binding of clients to the surface of condensates, but addition of rapamycin recruited FRB-GFP-ELK1 and FRB-mCherry-MAPK3 into the condensates (Figures 1A, 1D, and S1B).

Upon ELK1 and MAPK3 recruitment into condensates, phosphorylation of $ELK1^{WT}$ increased by 22% compared with control (Figure 1E). The $ELK1^{DM}$ mutant had lower baseline phosphorylation, as expected, but the relative increase rate upon recruitment into condensates nearly doubled (Figures 1E and S1C). Together, these results indicate that recruitment of MAPK3 kinase and the ELK1 substrate into a condensed phase accelerates phosphorylation, especially for substrates that lack docking motifs. The reaction acceleration in this experiment appears relatively small (22% for $ELK1^{WT}$, 91% for $ELK1^{DM}$); however, the condensate phase only constituted a tiny fraction of the total reaction volume (less than 3%). Therefore, as previously reported, for similar experiments (Peeples and Rosen, 2021), we

(G) Recruitment to condensates increased phosphorylation levels *in vivo*. Top: micrographs *S. cerevisiae* cells with various combinations of $MAPK3^{DM}$ (green), ELK1 (red), and scaffold controls or $SUMO_{10}$-SIM_6 condensates (no fluorescent tag). Scale bars, 5 μm. Bottom: representative western blots for ELK1-S383 phosphoepitope; total ELK1; activation-loop phosphates on the MAPK3 kinase (pT202/pY204), and tubulin loading control. Red arrowheads indicate hypershifted bands. Quantification of ELK1 S383 phosphorylation (pS383) and the hyperphosphorylation (hypershift/tubulin) are shown in bottom graphs. For S383 phosphorylation, band intensities of total phosphorylated ELK1 were normalized to total ELK1 levels, and this value was further normalized to the phosphorylation level of ELK1 in the control strain (leftmost). For hyperphosphorylation (hypershift/tubulin) quantification, the intensity signal of hypershifted band (detected by anti-p-ELK1-S383) was normalized to tubulin levels in the bottom graph, and the values were further normalized to the control strain. Error bars indicate ± SD (n = 3). Statistical comparisons are by Tukey-Kramer test: *p < 0.05, **p < 0.01, ***p < 0.001, N.S., not significant.

believe the actual acceleration in condensates is far greater than apparent in the bulk reaction.

Recruitment to synthetic condensates increases phosphorylation *in vivo*

We next used the budding yeast *Saccharomyces cerevisiae* as a model system to see if synthetic condensates could potentiate phosphorylation *in vivo*. We expressed a single polypeptide consisting of $SUMO_{10}$ fused to SIM_6 ($SUMO_{10}$-SIM_6) (Banani et al., 2016). This approach ensures that there are excess SUMO domains available as client-binding sites within the condensate. Rapamycin changes the biophysical properties of *S. cerevisiae* (Delarue et al., 2018); therefore, we did not use the FKBP12/FRB system to recruit clients. Instead, we recruited the constitutively active $MAPK3^{R84S}$ kinase (henceforth simply referred to as MAPK3) and its substrate ELK1 by fusion of a single SIM motif to their C termini (Figure 1F). We expressed combinations of SIM-tagged $ELK1^{WT}$ or $ELK1^{DM}$ (henceforth $ELK1^{WT}$-SIM or $ELK1^{DM}$-SIM) with $SUMO_{10}$-SIM_6 in *S. cerevisiae* and analyzed phosphorylation levels by western blotting using an ELK1 Serine-383-phospho-specific antibody. We observed basal phosphorylation of ELK1-SIM without MAPK3-SIM expression, indicating that yeast kinases can phosphorylate ELK1-SIM at low levels. Co-expression of MAPK3-SIM slightly increased $ELK1^{WT}$-SIM phosphorylation (Figure S1D) but did not increase $ELK1^{DM}$-SIM phosphorylation levels in the absence of the $SUMO_{10}$-SIM_6 condensate (Figure 1G). However, $ELK1^{WT}$-SIM and $ELK1^{DM}$-SIM phosphorylation at S383 was substantially increased when co-recruited with MAPK3-SIM into condensates (3.8-fold and 4.9-fold, respectively, $p < 0.001$; Figure 1G, top graph, Figure S1D). Consistent with *in vitro* experiments, $ELK1^{DM}$-SIM showed a greater relative increase in phosphorylation upon condensate recruitment. To control for scaffolding effects (i.e., the simultaneous binding of MAPK3-SIM and ELK1-SIM to adjacent SUMO domains in the dispersed solute phase), we also used a SUMO dimer ($SUMO_2$) that did not form condensates. $SUMO_2$ expression did not significantly increase $ELK1^{WT}$-SIM or $ELK1^{DM}$-SIM phosphorylation, indicating that recruitment to a condensed phase was required for increased phosphorylation. Taken together, and combined with the *in vitro* results above, these experiments indicate that recruitment to condensates increases phosphorylation rates *in vivo*.

Interestingly, we observed an increase in ELK1-SIM phosphorylation in the presence of $SUMO_{10}$-SIM_6 even without MAPK3-SIM expression (Figure 1G), suggesting the possibility that endogenous yeast kinases may be recruited into these condensates. We searched for SIM motifs in yeast CMGC family members, which are primarily proline-directed serine/threonine kinases. Surprisingly, most of these kinases harbor putative SIM motif (Table S1; Beauclair et al., 2015). We focused on yeast MAPK family members and a CDK family member Pho85. We found that deletion of the MAP kinases *FUS3 or KSS1*, and the CDK *PHO85* partly reduced phosphorylation. A *fus3Δ*, *kss1Δ*, and *pho85Δ* triple knockout mutant completely lost the increase in ELK1-SIM phosphorylation in the presence of $SUMO_{10}$-SIM_6 condensates (Figure S1E). These results suggest that *Fus3p*, *Kss1p*, and *Pho85p* acquire the ability to phosphorylate ELK1-SIM upon recruitment to $SUMO_{10}$-SIM_6 condensates.

Recruitment to synthetic condensates leads to novel multi-site phosphorylation *in vivo*

In addition to increased intensity of phospho-ELK1 bands, we noticed prominent slower migrating species when clients were recruited to condensates. ELK1 is known to be phosphorylated at multiple sites by MAPK3. Therefore, we hypothesized that the slowly migrating bands on the western blot were due to multi-site phosphorylation. Lambda phosphatase treatment resulted in almost complete loss of the hypershifted bands, whereas phosphatase inhibitor addition maintained the hypershifted band, confirming that phosphorylation caused the slow migration pattern (Figure S1F). ELK1 contains eleven serines or threonines immediately followed by proline, corresponding to consensus MAPK3 phosphorylation sites (Cruzalegui et al., 1999). Substitution all of these serines/threonines (Figure S1G) with alanine (ELK1-11A mutant) led to the loss of almost all hypershifted bands (Figure S1H). Quantification of slow-migrating bands indicated a 220-fold increase in hyperphosphorylation when $ELK1^{DM}$-SIM was recruited to condensates (Figure 1G, bottom graph, $p < 0.001$) and a 380-fold increase in the hypershifted band for $ELK1^{WT}$-SIM (Figure S1D, bottom graph, $p < 0.001$). ELK1 was previously shown to be phosphorylated at different sites with different kinetics (Mylona et al., 2016). Serine 383 (Serine 384 in mouse Elk-1) is the most rapidly phosphorylated residue, perhaps leading to partial reaction saturation even when $ELK1^{WT}$-SIM and MAPK3-SIM are co-expressed without $SUMO_{10}$-SIM_6 and explaining the modest increase in phosphorylation of this residue when $ELK1^{WT}$-SIM is recruited to condensates. On the other hand, condensate recruitment seems to have a far more pronounced effect on the phosphorylation of residues that are normally inefficiently phosphorylated (Mylona et al., 2016). Therefore, we focused on these hypershifted bands for our study.

Condensates facilitate dynamic new links between kinases and substrates

We hypothesized that recruitment into condensates might create a permissive environment for phosphorylation, potentially expanding kinase specificity. To test this idea, we investigated whether other kinases that did not evolve with ELK1 as a substrate could phosphorylate ELK1-SIM when recruited to $SUMO_{10}$-SIM_6 condensates. We first selected Fus3, the yeast kinase most closely evolutionarily related to MAPK3 (Figure 2A). The addition of the α-factor mating peptide activates a signaling pathway that greatly increases Fus3 kinase activity (Elion, 2000). We first added a single SIM tag to the endogenous *FUS3* gene and found that α-factor caused a slight increase in ELK1-SIM phosphorylation as predicted (Figures S2A–S2D). However, recruitment to condensates was weak. We therefore tagged the *FUS3* gene with a double SIM tag (gene product hereafter, Fus3-2xSIM) to more strongly recruit it into $SUMO_{10}$-SIM_6 condensates (Figures 2B and S2A–S2D). Western blot results showed that ELK1-SIM phosphorylation on S383 increased ~7-fold when Fus3-2xSIM was co-localized in $SUMO_{10}$-SIM_6 condensates even prior to addition of α-factor (Figure 2B, top graph, third lane, $p < 0.01$). This result indicates that basal activity of Fus3-2xSIM can drive significant phosphorylation of a novel substrate in condensates. However, the level of ELK1-SIM S383 phosphorylation was further increased to ~15-fold above background upon activation of

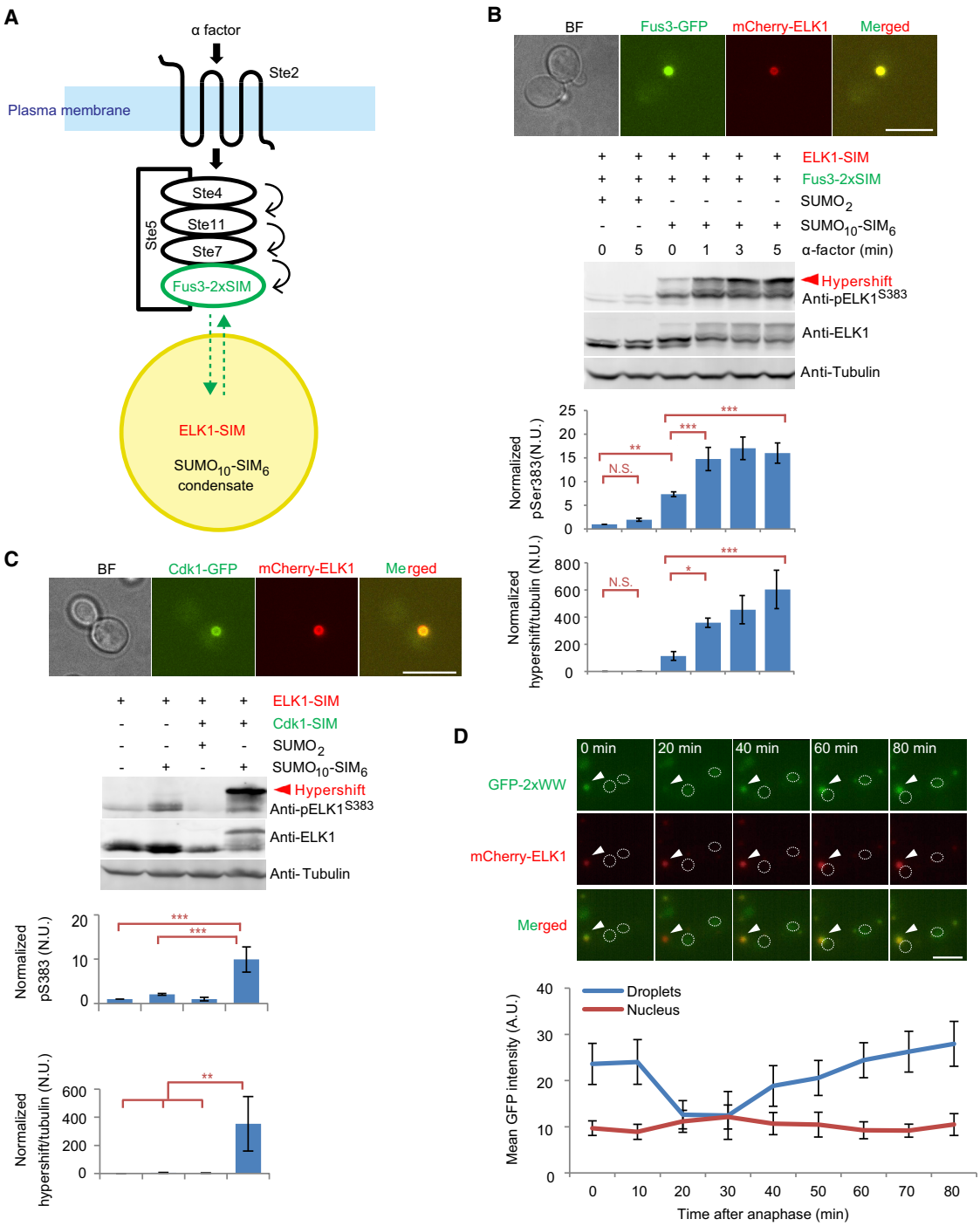

Figure 2. Condensates facilitate new links between kinases and substrates

(A) Schematic of ELK1 phosphorylation by Fus3 in condensates.

(B) Phosphorylation of ELK1 by Fus3 is accelerated in the condensed phase. Cells were treated with 2 μM α-factor to activate Fus3. Top: representative micrographs; bottom: representative western blots. Antibodies, quantification, and normalization of ELK1 S383 phosphorylation (pS383) and hyperphosphorylation (hypershift/tubulin) are as in Figure 1. n = 3.

(C) Phosphorylation of ELK1 by Cdk1 is accelerated in the condensed phase. Micrographs, western blots, and quantification are as in (B).

(D) The NLS-GFP-2xWW reporter dynamically changes localization during mitosis. Average projections of representative micrographs (GFP-2xWW, green; mCherry-ELK1, red) are shown. White dotted line indicates the position of the nucleus as detected by a 2xNLS-BFP reporter. White arrowheads indicate condensates. Mean intensities of GFP in condensates and in the nucleus are plotted. n = 10. Scale bars, 5 μm. Error bars indicate ± SD. Statistical comparisons are by Tukey-Kramer test, *p < 0.05, **p < 0.01, ***p < 0.001, N.S., not significant.

Fus3 by addition of α-factor for 5 min (Figure 2B, top graph, $p < 0.001$). Furthermore, the hypershifted bands were even more strongly induced by α-factor (~600-fold, $p < 0.001$, Figure 2B, bottom graph). Expression of ELK1-SIM and Fus3-2xSIM together with a simple $SUMO_2$ scaffold did not result in significantly increased phosphorylation of ELK1-SIM, regardless of α-factor addition. These results indicate that a novel kinase-substrate connection can be induced by recruitment to a condensate and that information from upstream signaling can still be received within this condensed phase within 1 min.

In processive phosphorylation, multiple phosphorylation events occur in a single kinase/substrate interaction (where a scaffold can also be considered part of the interaction), whereas in distributive phosphorylate, phosphates are added to the substrate over the course of several interactions. The prediction of processive phosphorylation is that, in a time-course, the uppermost hyper-phosphorylated bands should appear immediately and then get more abundant with time (Kõivomägi et al., 2011). The prediction of distributive phosphorylation is that intermediate bands should appear first and then higher and higher bands appear over time in a ''ladder-like'' fashion. We found that Fus3 activation led to immediate appearance of a completely hypershifted band (after 1 min) that proceeded to gets darker. There was no significant accumulation of intermediate phosphorylated forms after α-factor addition at 1 or 3 min, indicating that ELK1-SIM phosphorylation in $SUMO_{10}$-SIM_6 condensates was processive (Figures 2B, S2D, and S2E).

Next, we tested if a more evolutionarily distant kinase could phosphorylate ELK1-SIM within condensates. We chose the CDK Cdk1 (encoded by the *CDC28* gene in *S. cerevisiae*). Cdk1 is still proline directed but is structurally and functionally distinct from MAP kinases and recognizes different docking motifs (Howard et al., 2014; Mok et al., 2010; Schulman et al., 1998). We tagged the endogenous Cdk1 with a single SIM peptide (Cdk1-SIM) and observed robust recruitment into $SUMO_{10}$-SIM_6 condensates (Figure 2C, top). Co-recruitment of ELK1-SIM and Cdk1-SIM led to high levels of phosphorylation of ELK1-SIM, both in terms of S383 phosphorylation (~10-fold increase, $p < 0.001$; Figure 2C, top graph) and levels of hypershifted bands (~300-fold increase, $p < 0.01$; Figure 2C, bottom graph). Expression of ELK1-SIM and Cdk1-SIM together with a simple $SUMO_2$ scaffold did not increase ELK1-SIM phosphorylation over background levels.

To gain insight into the kinetics of this reaction, we engineered an induced dimerization system based on plant gibberellic acid (GA) signaling (Miyamoto et al., 2012) to recruit clients into $SUMO_{10}$-SIM_6 condensates in *S. cerevisiae* cells (Figure S2F). GA addition induced mCherry-ELK1 recruitment into $SUMO_{10}$-SIM_6 condensates in which Cdk1-GFP-SIM was localized (Figure S2G) and increased ELK1 phosphorylation (Figure S2H). The GA-induced reaction was slower than Fus3, and hypershifted bands were only significantly induced after 30 min. Nevertheless, as for the Fus3 system, there was no ladder-like accumulation of intermediate phosphorylated forms detected after GA addition but rather the hypershifted band appeared immediately and grew more intense with time, consistent with a processive multi-site phosphorylation reaction.

Cdk1 regulates the cell division cycle (Malumbres, 2014). Cdk1 is most active during mitosis and is inactivated during mitotic exit by degradation of cyclins (Enserink and Kolodner, 2010). In addition, the CDC14 phosphatase that counteracts Cdk1 is specifically activated during mitotic exit (Stegmeier and Amon, 2004). Therefore, substrates of Cdk1 are dynamically phosphorylated and dephosphorylated as the cell cycle progresses. To further investigate the ability of synthetic condensates to create novel kinase connections while allowing dynamic regulation, we built a reporter system to visualize phosphorylation of ELK1-SIM by Cdk1 in real time in single cells.

To create a live-cell reporter of ELK1-SIM phosphorylation, we fused two WW domains from the *Homo sapiens* PIN1 protein to GFP (GFP-2xWW). The WW domain specifically interacts with phosphorylated serine-proline motifs (Verdecia et al., 2000). We hypothesized that ELK1-SIM phosphorylation within synthetic condensates would create WW-domain binding sites leading to reporter recruitment to the condensates (Figure S3A). Indeed, we found that co-expression of MAPK3-SIM and ELK1-SIM led to the translocation of the GFP-2xWW reporter into $SUMO_{10}$-SIM_6 condensates (Figure S3B, top). As a control, we expressed a catalytically dead MAPK3 mutant (MAPK3-K71R) and found very little recruitment of the reporter into $SUMO_{10}$-SIM_6 (Figures S3B, bottom and S3C). These results suggested that the reporter was recruited to synthetic condensates in a phosphorylation-dependent manner.

We next modified the reporter to attempt to reveal dynamic phosphorylation of ELK1-SIM by Cdk1. We added an SV40 nuclear localization signal (NLS) to the N terminus (NLS-2xWW-GFP), such that when the reporter and ELK1-SIM were co-expressed with $SUMO_{10}$-SIM_6 but Cdk1 was not tagged with SIM, most of the reporter was nuclear, and very little was recruited to condensates (Figure S3D). However, when Cdk1 was tagged with SIM, a significant number of cells had strong reporter recruitment to condensates (Figure S3E). We next examined the dynamics of reporter recruitment to condensates during the cell cycle by time-lapse imaging (Figure 2D). Reporter intensity within condensates was highest immediately prior to anaphase, the point at which Cdk1 activity is highest (Enserink and Kolodner, 2010). Approximately 20–30 min after anaphase, reporter signal was reduced within condensates and relocalized to the nucleus (Figure 2D; Video S1). This corresponds to the timing of mitotic exit, when Cdk1 is rapidly inactivated by cyclin degradation and expression of the Cdk1 inhibitor Sic1 (Enserink and Kolodner, 2010). In addition, the phosphatase Cdc14 is activated at this time, leading to rapid dephosphorylation of phosphorylated S-P and T-P motifs (Visintin et al., 1998). Subsequently, after 10–20 min, a time when Cdk1 activity is rising, the reporter intensity in condensates also started to increase (Figures 2D and S3F). Collectively, these results suggest that recruitment of Cdk1-SIM to a synthetic condensate can create a new kinase-substrate connection, with dynamics that closely follow the cell cycle.

We next wondered if recruitment to condensates would relax the primary specificity of kinases, enabling phosphorylation of a broader range of peptides. First, we used a short peptide flanking serine383 in ELK1 as a substrate (residues 370–394, referred to as min383 hereafter) to completely remove the D box and F box docking sites. We fused this peptide and MAPK3 to a 5xSIM tag

to obtain strong enrichment within condensates (Figure S4A). This resulted in strong phosphorylation (Figures S4B–S4D), suggesting that docking motifs are not required for MAPK3 phosphorylation within condensates. Interestingly, condensates were also formed when 5xSIM-tagged-clients were co-expressed with $SUMO_2$ (Figure S4C), resulting in increased min383 phosphorylation, and these condensates also drove phosphorylation.

We noticed that there were multiple hypershifted bands, accounting for almost 50% of total min383 (Figure S4D) within $SUMO_{10}$-SIM_6 condensates. These bands disappeared after lambda phosphatase treatment (Figure S4E), suggesting that phosphorylation caused this slow migration pattern. There is only one additional MAPK3 consensus phospho-acceptor site (S/T-P motif, serine389) in min383 (Figure S4F); therefore, we hypothesized that other non-consensus sites could also be phosphorylated. We generated point mutant and truncation constructs to identify the residues responsible for the hypershifted bands (Figure S4G). Deletion of four consecutive serines at the N terminus almost completely abolished slowly migrating bands (Figure S4H), suggesting that these four non-consensus serines were phosphorylated by MAPK3. Thus, MAPK3 can phosphorylate non-consensus sequences when within condensates.

We next investigated the ability of Cdk1 to phosphorylate non-canonical substrates within condensates. Cdk1 is also a proline-directed kinase; hence, we generated a synthetic construct that fused short peptides from the human P53 and RPS6 proteins (Figures S4I and S4J, referred to PR hereafter), none of which contain any known primary specificity determinants for Cdk1 (Mok et al., 2010). Western blot results showed that peptides from serine9 and serine37 in P53 were more highly phosphorylated by Cdk1 when recruited to condensates (Figures S4K–S4M). Serine235/236 in RPS6 was also phosphorylated by Cdk1 in condensates. Note, in some cases, we believe that recruitment into synthetic condensates stabilizes clients, for example, leading to the high anti-HA signal in lanes 3 and 5 of Figure S4L. To control for these effects, we normalized the phosphorylation signal to the total anti-HA signal. Collectively, these results show that the primary specificity of MAPK3 and Cdk1 is relaxed when recruited to condensates.

Multiple factors contribute to hyperphosphorylation in condensates

A major advantage of synthetic biology is the possibility of systematically varying parameters in an attempt to understand general principles. Therefore, we varied the properties of both the condensate scaffold proteins and the clients to investigate which factors impact phosphorylation of ELK1 by MAPK3 within condensates (Figures 3A and 3B).

First, we characterized the effect of client-binding affinity on phosphorylation in condensates. A single substitution in the SIM peptide (substitution of Isoleucine 9 with proline, referred to as SIM^{I9P} hereafter) decreases the affinity of the interaction between SIM and SUMO (Namanja et al., 2012). We tagged the ELK1 substrate with either WT SIM (SIM^{WT}) or SIM^{I9P}, whereas the MAPK3 kinase was always tagged with SIM^{WT}. The concentration of ELK1-SIM^{I9P}-tagged substrate was dramatically reduced in $SUMO_{10}$-SIM_6 condensates (Figures 3B and S5A). Western blotting showed that hyperphosphorylation of ELK1-SIM^{I9P} in condensates was reduced by almost 80% compared with ELK1-SIM^{WT} (Figures 3B and S5B). We hypothesized that the reduced substrate concentration led to the decreased hyperphosphorylation. To test this idea, we used a stronger promoter to increase the expression level of ELK1-SIM^{I9P} and restore the concentration of ELK1-SIM^{I9P} in condensates. Indeed, this higher substrate concentration within condensates partly restored ELK1-SIM^{I9P} hyperphosphorylation. However, when ELK1-SIM^{I9P} was present at equivalent concentration to ELK1-SIM^{WT}, there was still a 2-fold decrease in hyperphosphorylation. One possible explanation is that the binding kinetics of client SUMO domains within the condensate plays an important role. The unbinding rate (k_{off}) of ELK1-SIM^{I9P} is likely to be higher than ELK1-SIM^{WT}. Therefore, we speculated that lower k_{off} might favor hyperphosphorylation. Increasing valency can also reduce k_{off} (Tang et al., 2012). We therefore fused both kinase and substrate with two SIM-tags (2xSIM) to investigate the effect of client valence on hyperphosphorylation in condensates. The 2xSIM-tag led to a slightly higher (~20%) MAPK3 concentration in condensates compared the single SIM tag but had no effect on ELK1 concentrations (Figures 3B and S5A). However, western blotting showed that ELK1 hyperphosphorylation almost doubled (Figures 3B and S5B). We compared the 2xSIM-tagged substrate phosphorylation to strongly overexpressed kinase and substrate with a single SIM tag. This strong overexpression led to higher client concentrations in condensates and slightly higher ELK1 hyperphosphorylation. Together, these results suggest that both client concentration and binding kinetics modulate the degree of hyperphosphorylation within condensates.

The number of excess client-binding sites strongly impacts hyperphosphorylation

We next investigated how the properties of synthetic condensates could impact hyperphosphorylation. The presence of excess SUMO domains within the $SUMO_{10}$-SIM_6 condensates has been shown to be important for client recruitment (Banani et al., 2016). We therefore tested the effect of reducing the number of free SUMO domains by comparing $SUMO_7$-SIM_6 to $SUMO_{10}$-SIM_6 condensates. We screened for cells with client recruitment into $SUMO_7$-SIM_6 condensates that were similar to $SUMO_{10}$-SIM_6 condensates (Figures 3B and S5A). However, ELK1-SIM hyperphosphorylation within $SUMO_7$-SIM_6 condensates was reduced by almost 90% (Figures 3B and S5B). Next, we asked whether we could restore hyperphosphorylation in $SUMO_7$-SIM_6 condensates by increasing client concentration in condensates. Interestingly, hyperphosphorylation was still ~3-fold lower in strains expressing $SUMO_7$-SIM_6 condensates when the expression of both clients was increased such that client concentration in $SUMO_7$-SIM_6 was higher than in $SUMO_{10}$-SIM_6 condensates. This suggests that the excess SUMO domains in condensates potentiates hyperphosphorylation through a mechanism beyond simple mass action.

Condensate scaffold flexibility is crucial for hyperphosphorylation

The SUMO-SIM condensates are based on highly flexible polymers that can assemble in many conformations. We wondered whether this flexibility, which appears to be a frequent feature

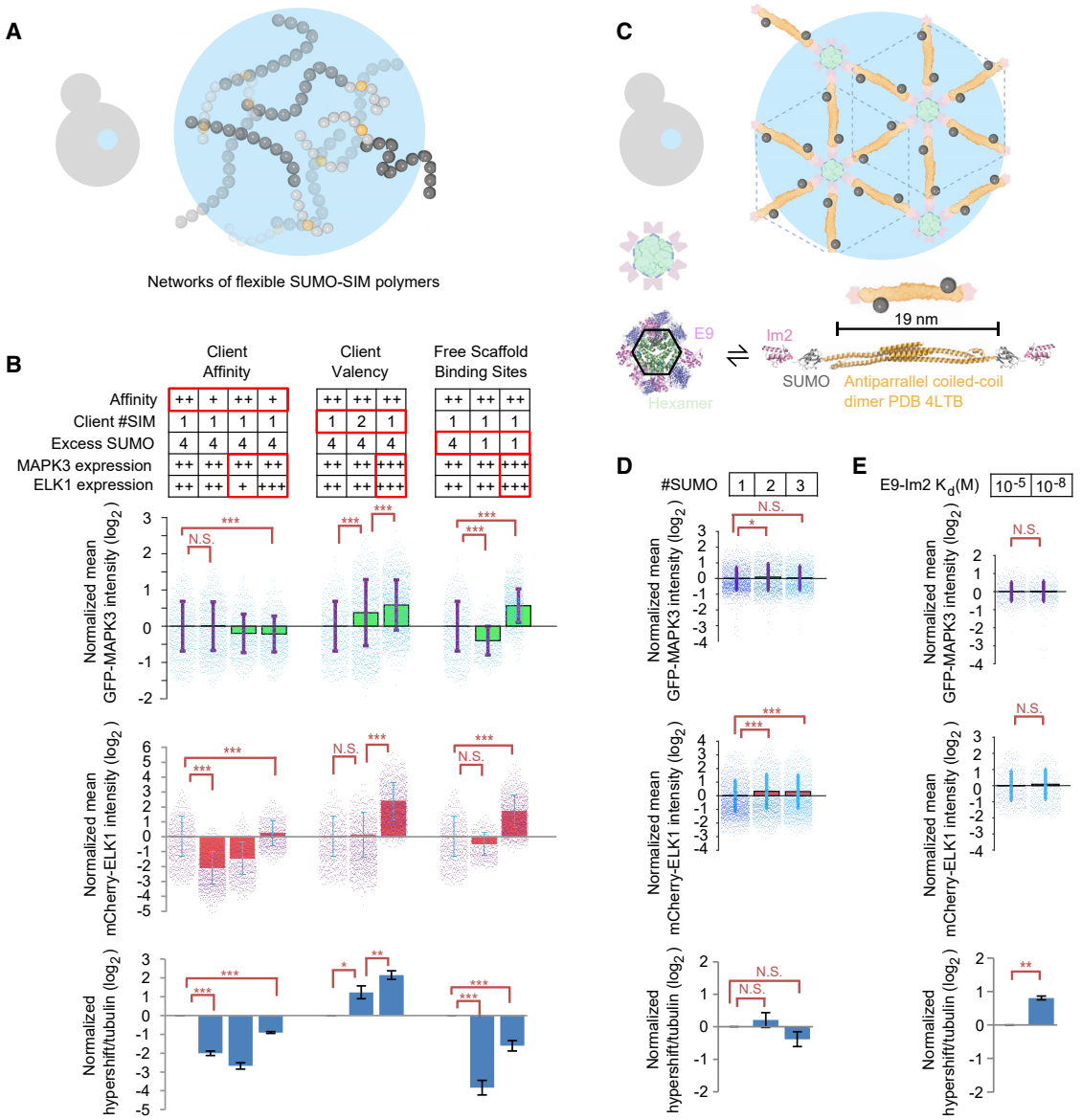

Figure 3. Multiple factors contribute to hyperphosphorylation in condensates

(A) Schematic of $SUMO_n$-SIM_n condensates in *S. cerevisiae* cells.

(B) Affinity: interaction strength altered using SIM variants with low K_d (higher affinity, ++) or high K_d (lower affinity, +). Client # SIM: one or two SIMs on clients. Excess SUMO: $SUMO_{10}$-SIM_6 has 4 excess SUMO per scaffold, and $SUMO_7$-SIM_6 has 1 excess SUMO per scaffold. MAPK3 expression; ELK1 expression: different promoters for high (+++), medium (++), or low expression levels (+). Relative concentrations of clients within condensates are shown in red and green bar graphs, where each point is the quantification of one condensate. Bottom: blue bar graph shows the quantification of hyperphosphorylation levels from western blots. Values normalized to the median of the leftmost strain.

(C) Schematic of a synthetic two-component condensate. One component consists of a homodimerizing scaffold fused to one or more SUMO to recruit SIM-tagged client proteins and an Im2 domain. The other component consists of a homohexamerizing scaffold fused to BFP and an E9 domain. The Im2 and E9 domains interact with one another.

(D) One, two, or three SUMO domains were inserted into the dimer-forming component. Client concentrations within condensates were estimated as above and normalized to leftmost strain. Bottom: blue bar graph shows the quantification of hyperphosphorylation levels from western blots.

(E) Characterization of the effect of the affinity of the Im2/E9 interaction. Client concentrations and hyperphosphorylation quantified as above. n = 3 for all experiments. Error bars indicate ± SD; statistics in 3B and 3D by Tukey-Kramer test, statistics in 3E by Student's t test, *p < 0.05, **p < 0.01, ***p < 0.001; N.S., not significant.

of biological condensates (Alberti and Hyman, 2021; Hastings and Boeynaems, 2021; Li et al., 2012), was important for the potentiation of phosphorylation. We took advantage of a recently described design strategy (Heidenreich et al., 2020) based on a well-structured synthetic two-component system (Figure 3C). One component consists of a homo-hexamer. The other component is a homo-dimer consisting of a long (18 nm), rigid, antiparallel coiled-coil domain from the TRIM25 protein. Interaction between these two components was engineered using a well-characterized heterodimeric interaction between the colicin E9 (henceforth simply E9) and the immunity protein, Im2 (Li et al., 1998). We fused E9 to the C terminus of the hexamer and Im2 to the N terminus of the dimer. An important design feature is that the dimer is too long to bind twice to the same hexamer, thereby making lattice assembly within the condensate more predictable. We additionally fused a SUMO domain to the N terminus of the dimer. The topology of the dimer is such that the N termini are distant from one another at the opposite ends of each dimer. This synthetic condensate is predicted to assemble in a limited set of local geometries from rigid components that hold individual SUMO domains relatively distant from one another.

When expressed in yeast, the synthetic two-component-system-formed condensates that recruited ELK1-SIM and MAPK3-SIM clients (Figure S5C). We screened for yeast strains that recruited clients to these two-component-system-formed condensates at similar levels as SUMO-SIM condensates (Figure S5D). We found that recruitment of ELK1-SIM and MAPK3-SIM to SUMO domains within this ordered condensate led to a slight increase in total phosphorylation levels at S383 (~50%) and a similar increase hyperphosphorylation (~35-fold) (Figure S5E) to $SUMO_7$-SIM_6, but ~10-fold less than in $SUMO_{10}$-SIM_6 condensates. Thus, scaffold flexibility appears to be important for efficient phosphorylation within condensates.

Three adjacent client-binding sites are insufficient for efficient phosphorylation in rigid condensates

A major feature of the two-component system is that the SUMO binding sites are held at a slight distance from one another within a relatively rigid network. This is distinct from the SUMO-SIM condensates, where multiple adjacent SUMO domains can be available for client binding in a single polymer, and the scaffold flexibility potentially allows for even more extensive clusters of SUMOs to occur. Indeed, the fact that the availability of excess SUMO domains has the largest effect on the efficiency of hyperphosphorylation (Figure 3B, right) suggests that the availability of local clusters of client-binding sites is crucial for efficient condensed-phase signaling. Control experiments demonstrate that dimers of SUMO in solution are insufficient for reaction acceleration (Figures 1G, 2B, 2C, and S1D) Hence, we investigated if adding pairs or triads of SUMO domains to the dimer in the two-component condensate could better drive condensed-phase phosphorylation. We screened for cells with similar client concentrations within condensates to simplify interpretation (Figure S5E). We fused the dimer component to 2xSUMO and 3xSUMO. Again, each 2xSUMO or 3xSUMO is held 18 nm distant from its partner by the rigid antiparallel coiled-coil of the dimer and can be within 9–12 nm of a set of SUMO sites on an adjacent dimer head (Figure 3C). We found no increase in S383 phosphorylation or hyperphosphorylation of ELK1-SIM with 2xSUMO or 3xSUMO relative to 1xSUMO within these rigid condensates (Figures 3D and S5F). These results suggest that even with a huge concentration of 3xSUMO domains, the inability of the rigid scaffold network to generate larger SUMO clusters may limit the efficiency of this condensate as a catalyst of hyperphosphorylation. Therefore, local pockets of high client-binding site concentration (>3 SUMO sites), and perhaps scaffold polymer dynamics *per se*, may play an important role in condensed-phase signaling.

Scaffold material properties do not greatly affect phosphorylation within ordered condensates

A useful feature of the two-component system is the availability of Im2 variants with varying affinity to E9 (Heidenreich et al., 2020; Li et al., 1998). We engineered two interaction strengths between the two scaffold components, either in the micromolar ($K_d \sim 3 \times 10^{-5}$ M) or nanomolar ($K_d \sim 1.2 \times 10^{-8}$ M) range. This approach was previously shown to create liquid- and solid-like condensates, respectively (Heidenreich et al., 2020). We screened for yeast strains expressing each of these variants that had similar condensate sizes and client concentrations in the condensates (Figures 3E and S5G). Western blotting showed a slight increase (~2-fold) in hyperphosphorylation in the strain expressing the high-affinity (10^{-8}M) Im2 variant over that of the lower affinity (10^{-5}M) variant (Figures 3E, VG, and S5H). This result suggests the material states and dynamics of the condensed scaffold only play a minor role in condensed-phase phosphorylation within these well-structured networks.

Synthetic condensed-phase signaling can respond to osmotic compression

Osmotic compression reduces cell size, increases macromolecular crowding, and decreases molecular diffusion. On a microscopic scale, the assembly, dynamics, and network structure of condensates could all be impacted by macromolecular crowding, as could the dynamics of client interactions and motion within the condensed phase. We speculate that client molecules exist in two states within condensates: some in the fluid phase that permeates the condensate, others bound to the condensate scaffolds. As macromolecular crowding alters the condensate network, both the motion through the fluid phase and the binding kinetics of clients could be impacted. Thus, it is possible that phosphorylation within condensates could be sensitive to changes in the biophysical properties of the cell and provide a mechanism to convert physical states such as macromolecular crowding to chemical signals. We took advantage of our synthetic condensates to test this idea and investigate factors important for this physical sensing.

We used *hog1Δ* strains that are deleted for the main osmotic stress response kinase. This mutation prevents osmoadaption and mitigates changes in signaling due to *Hog1p* activation upon osmotic stress (Hohmann, 2002). We tested condensates that varied in the two factors that we previously determined to have the greatest effect on phosphorylation efficiency: condensate network flexibility, and the availability of excess SUMO (i.e., $SUMO_{10}$-SIM_6 versus $SUMO_7$-SIM_6).

First, we tested the effect of osmotic compression of $SUMO_{10}$-SIM_6 condensates. We osmotically compressed cells with 1M

sorbitol for 1 h and quantified client recruitment, condensate size, and hyperphosphorylation of ELK1-SIM. Average condensate area decreased by around 35%, likely due to oncotic compression, and recruitment of GFP-MAPK3-SIM increased ~70% (Figures S6A and S6B), but ELK1-SIM hyperphosphorylation was only increased about 10% (Figure S6C, lanes 3 and 4). We reasoned that this could be because $SUMO_{10}$-SIM_6 condensates already give the most efficient hyperphosphorylation of any synthetic condensate; therefore, the reaction is essentially saturated and difficult to further accelerate. We therefore next tested the effect of osmotic compression of $SUMO_7$-SIM_6 condensates. The change in condensate area and client concentration was similar to that in $SUMO_{10}$-SIM_6 condensates (35% area decrease and ~70% increase in GFP-MAPK3-SIM; Figures S6A and S6B). However, the degree of ELK1-SIM hyperphosphorylation in $SUMO_7$-SIM_6 condensates was increased ~2-fold (Figure S6C, lanes 1 and 2). In conclusion, hyperphosphorylation within the efficient $SUMO_{10}$-SIM_6 condensates is relatively insensitive to osmotic compression, but hyperphosphorylation becomes sensitive to osmotic stress within the less efficient $SUMO_7$-SIM_6 condensates.

When *HOG1* is deleted, crosstalk from osmotic stress pathway to the *Fus3* kinase has been reported (O'Rourke and Herskowitz, 1998). We demonstrated above that *Fus3* can phosphorylate ELK1-SIM when recruited to condensates (Figure 2B). Therefore, it was important to rule out the possibility that osmotic stress leads to activation of *Fus3* and its recruitment to condensates. However, ELK1-SIM hyperphosphorylation increased similarly upon osmotic shock in *hog1Δ; fus3Δ* double-mutant strains and *hog1Δ* strains (Figure S6D). Therefore, *Fus3* does not appear to play a role in the change in hyperphosphorylation that we observe after osmotic compression.

In a control strain containing a soluble $SUMO_2$ scaffold control without condensates, osmotic shock led to reduced levels of mCherry-ELK1-SIM (Figure S6E). In cases with significant changes in ELK1-SIM levels, we normalized phosphoELK1-SIM levels to total ELK1-SIM levels to allow for meaningful comparisons. ELK1-SIM S383 phosphorylation was almost undetectable upon sorbitol treatment in the $SUMO_2$ scaffold control strain. Additionally, we tested a $SUMO_2$ scaffold control in which SUMO was fused the coiled-coil domain from TRIM25. The levels of ELK1-SIM S383 phosphorylation relative to total ELK1-SIM protein were decreased by almost 80% in this soluble $SUMO_2$ dimer scaffold strain (Figure S6F). This decrease may be caused by reduced molecular diffusion upon the increase in macromolecular crowding. There was less change in ELK1-SIM levels in all strains that recruited mCherry-ELK1-SIM to condensates. ELK1 is known to be regulated through proteolysis (Evans et al., 2011); therefore, we speculate that condensates can protect ELK1 from proteolysis.

The initial client concentration was higher in $SUMO_{10}$-SIM_6 condensates than in $SUMO_7$-SIM_6 condensates (Figure S6A). This led to the hypothesis that the hyperphosphorylation is almost saturated in $SUMO_{10}$-SIM_6 condensates, whereas $SUMO_7$-SIM_6 condensates remain sensitive to concentration changes. To test this idea, we used stronger promoters to increase client concentration in $SUMO_7$-SIM_6 condensates. Consistent with the hypothesis, there was no significant change in ELK1-SIM hyperphosphorylation upon osmotic compression in these strains (Figure S6C, lanes 5 and 6). Therefore, condensed-phase signaling can respond to osmotic compression when the system is appropriately tuned; hyperphosphorylation responds to osmotic compression within $SUMO_7$-SIM_6 condensates that contain a low enough client concentration that reaction rates are not saturated.

Next, we investigated the effect of osmotic compression on phosphorylation within the more rigid two-component condensates. We used the lower affinity Im2 variant that creates a more liquid-like condensate, which we reasoned would be more likely to respond to compression (Heidenreich et al., 2020). Upon osmotic compression, condensate area was only slightly decreased (~10%; Figure 4C), but the concentration of GFP-MAPK3-SIM clients increased in the condensates to a similar degree as in $SUMO_7$-SIM_6 condensates, by ~60% (Figure 4B). Strikingly, osmotic compression did not increase hyperphosphorylation in the two-component condensates but rather the degree of ELK1-SIM hyperphosphorylation was decreased by ~50% upon osmotic compression ($p < 0.05$; Figures 4D and 4E). We screened for colonies with a lower concentration of clients in two-component condensates to rule out the possibility that the phosphorylation rates were initially saturated. The degree of hyperphosphorylation in these strains was still reduced upon osmotic compression (Figures S6G and S6H). We also compared client recruitment between flexible $SUMO_7$-SIM_6 and the more rigid two-component condensates. The recruitment difference is small between the two condensates: mCherry-ELK1-SIM recruitment was similar, whereas GFP-MAPK3-SIM was recruitment to $SUMO_7$-SIM_6 condensates was ~65% that of two-component condensates (Figures S7A and S7B). Together, these results suggest that rigid condensates respond to osmotic compression in the opposite way to flexible condensates and suggest that the flexibility of SUMO-SIM condensates is important for their ability to transduce osmotic stress to changes in hyperphosphorylation.

To further investigate the hypothesis that structural rigidity explains the opposite response of the two-component condensates to osmotic compression, we modified this two-component system to connect each hexamer subunit with a flexible $SUMO_{10}$ polypeptide. In place of the Im2-E9 interaction, we simply placed a SIM peptide at the C terminus of the hexamer subunits, such that the network was crosslinked by SUMO-SIM interactions (Figure S7C). Co-expression of the hexamer-SIM with $SUMO_{10}$ led to condensate formation and client recruitment (Figure S7D). The area of these condensates area was reduced by 25% upon sorbitol treatment, significantly more than that for rigid two-component condensates ($p < 0.001$; Figures 4C and S7E). This increase in condensate compression is consistent with the idea that polymer flexibility is important for mesoscale structural changes to synthetic condensates upon changes to the physical environment. Western blotting showed that the relative amount of ELK1-SIM hyperphosphorylation in the hexamer-SIM + $SUMO_{10}$ condensate slightly increased, but not significantly (Figures 4D and 4E). Therefore, this mixed system with one structured and one flexible component shows intermediate behavior. These results further support the hypothesis that condensate

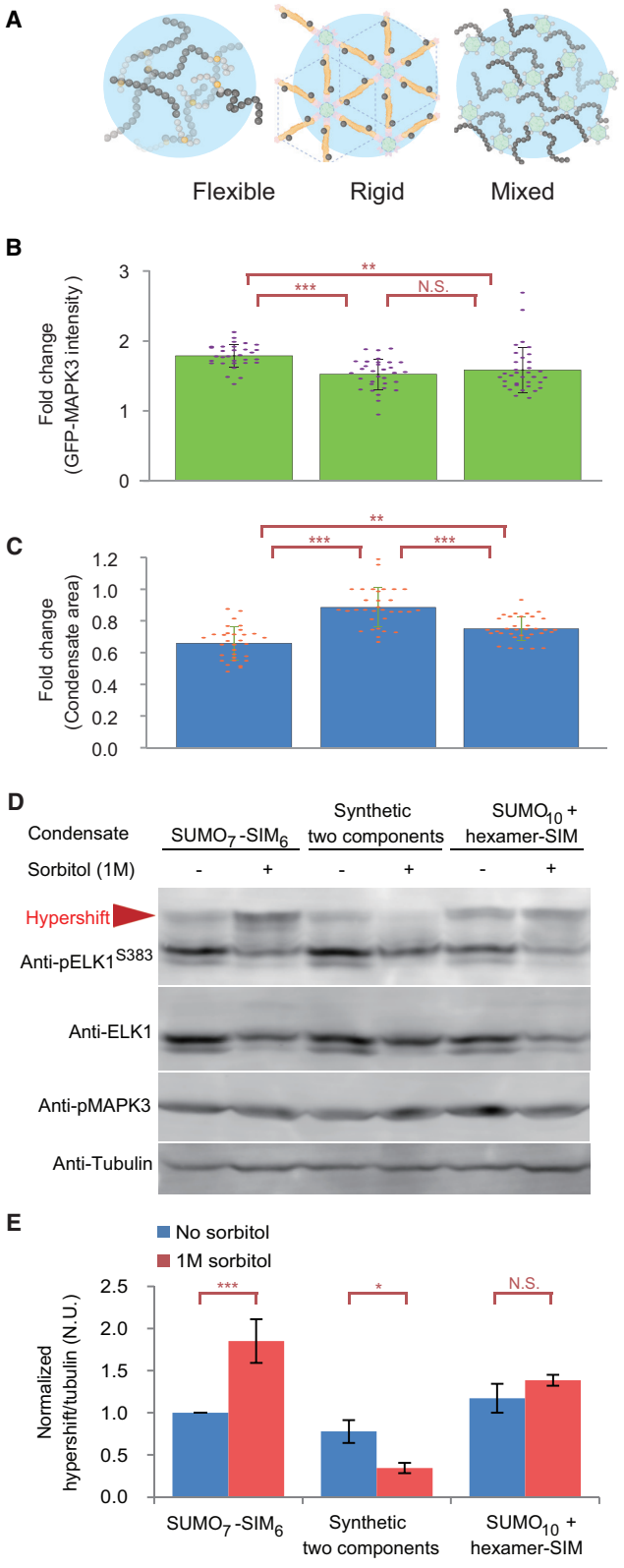

Figure 4. Synthetic condensed-phase signaling can respond to osmotic compression

(A) Schematic showing three different types of synthetic condensate: (left) rigid two-component condensate, (middle) flexible $SUMO_7$-SIM_6 condensate, and (right) mixed system.

(B) GFP intensity in condensates before and after 1 h osmotic compression with 1 M sorbitol.

(C) Condensate volumes decrease to varying degrees upon osmotic compression, depending on scaffold flexibility. Same condensates were measured before and after 1 h osmotic compression with 1 M sorbitol.

(D) Representative western blots.

(E) Osmotic compression increases hyperphosphorylation in flexible condensates and decreases hyperphosphorylation in rigid condensates. Quantification of degree of hyperphosphorylation from western blots, normalized as in previous figures. *hog1Δ* strains were used to prevent osmoadaptation. Error bars indicate ± SD (n = 3). Statistical comparisons are by Tukey-Kramer test: *p < 0.05, **p < 0.01, ***p < 0.001, N.S., not significant.

compressibility and scaffold linker flexibility are important for the response of condensed-phase phosphorylation to osmotic compression.

Synthetic condensed-phase signaling responds to changes in macromolecular crowding

We next investigated macromolecular crowding as a possible mechanism osmotic sensing by $SUMO_7$-SIM_6 condensates. We previously found that the mTORC1 pathway influenced the phase separation of $SUMO_{10}$-SIM_6 synthetic condensates through modulation of the concentration of ribosomes in the cytosol (Delarue et al., 2018). Ribosomes are the main mesoscale crowder in the cytosol. When mTORC1 is inhibited by rapamycin, the concentration of ribosomes decreases ~2-fold, and the phase separation of $SUMO_{10}$-SIM_6 is substantially reduced (Delarue et al., 2018). A similar effect is observed in the *sfp1Δ* mutant, which lacks the *Sfp1p* transcription factor that drives high levels of ribosome biogenesis downstream of active mTORC1; this mutant has low baseline crowding and therefore low $SUMO_{10}$-SIM_6 phase separation. Rapamycin has no further effect on ribosome concentration in this mutant, but crowding and condensation can be rescued by osmotic compression. We explored these conditions and mutants to test the hypothesis that condensed-phase signaling in $SUMO_7$-SIM_6 condensates respond to changes in macromolecular crowding.

We took advantage of 40-nm diameter genetically encoded multimeric nanoparticles (40nm-GEMs) to quantify macromolecular crowding (Delarue et al., 2018). We imaged cells at 100 Hz to obtain tracks of the motion of 40nm-GEMs (Figures 5A and 5B; Video S2). From the effective diffusion coefficient of 40 nm GEMs, we can infer properties of the intracellular environment, including the degree of macromolecular crowding at the length-scale of ribosomes. The Doolittle equation can be adapted to predict 40nm-GEM D_{eff} as a function of relative ribosome concentration and vice versa (Delarue et al., 2018; Doolittle, 1951). Using the same method (Figure S8A), we found that the baseline D_{eff} for W303 *hog1Δ* was 0.157 $\mu m^2\ s^{-1}$ (predicting 23 μM ribosomes) and that this value increased to ~0.462 $\mu m^2\ s^{-1}$ upon 2 h treatment with 1 μM rapamycin (Figure 5C), consistent with an almost one third reduction of ribosome concentration to 15.5 μM (Figure 5C). Deletion of *SFP1* (*sfp1Δ* mutant)

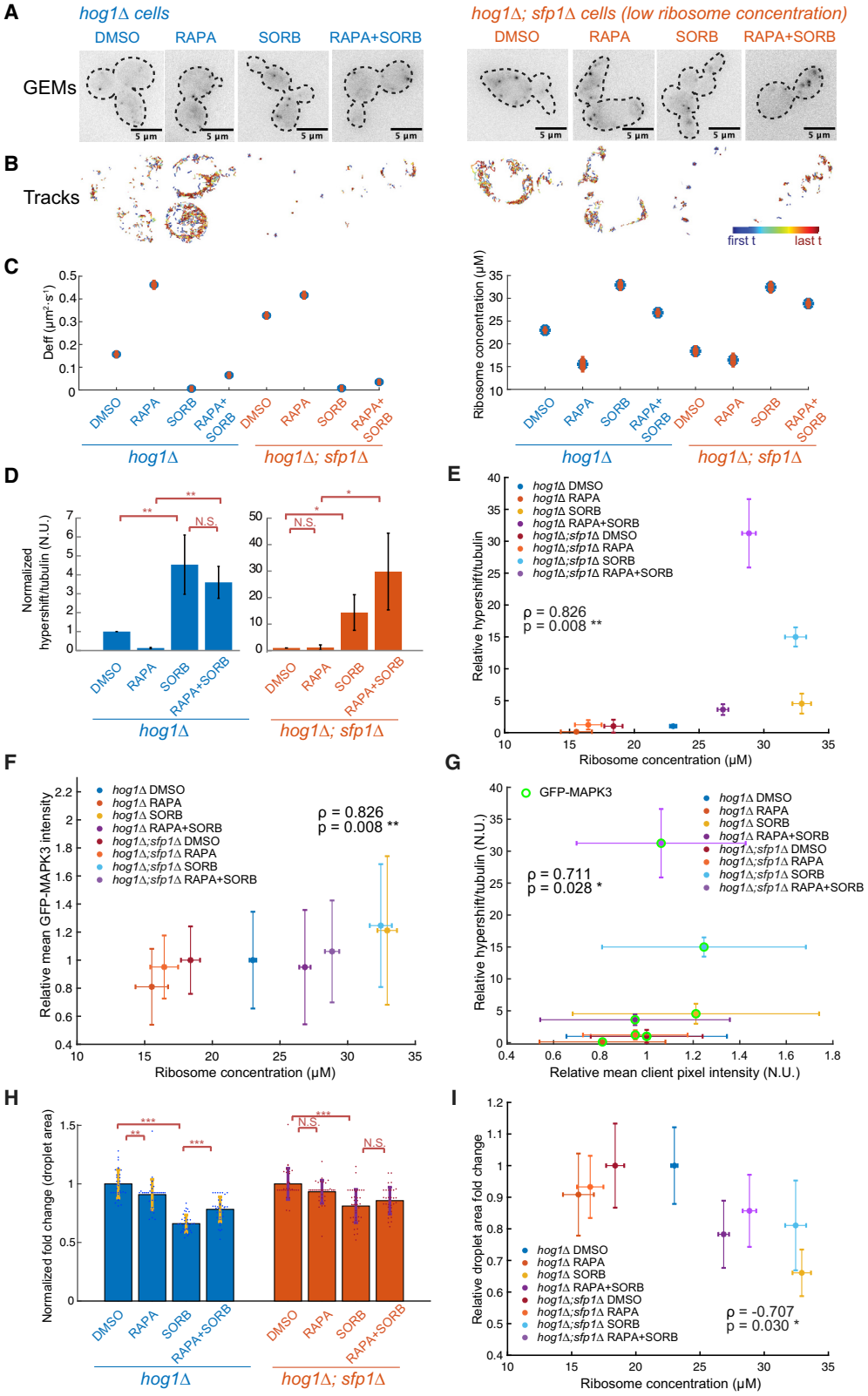

(legend on next page)

gave a similar decrease in ribosome concentration, to 16.4 μM, but in this case, without perturbation to mTORC1 kinase activity (Figure 5C). Osmotic compression of cells with 1M sorbitol for 1 h led to more than 10-fold decrease in 40nm-GEM D_{eff} in all conditions (Figures 5B and 5C), consistent with increased macromolecular crowding to ~ 32 μM ribosome concentration.

To prevent loss of condensates from dominating our results, we expressed sufficient $SUMO_7$-SIM_6 to favor condensate formation even when cytosolic crowding is reduced (Figure S8B). We then quantified hyperphosphorylation of ELK1-SIM in condensates in cells with different levels of crowding (Figures 5D and S8C). Note, total ELK1 levels were affected by rapamycin, osmotic compression, and *SFP1* deletion (Figure S8D); to control for this effect, phosphorylated ELK1 and hypershifted bands were normalized to total ELK1 levels. Hyperphosphorylation was reduced in conditions with decreased macromolecular crowding (e.g., 5-fold decease after rapamycin treatment) and increased in conditions with increased macromolecular crowding (e.g., >4-fold increase after osmotic compression). Plotting hyperphosphorylation as a function of ribosome concentration showed a significant positive correlation (Figure 5E; Spearman's rank $\rho = 0.826$, $p = 0.008 < 0.01$).

We considered mechanisms by which $SUMO_7$-SIM_6 condensates could sense crowding. Our first hypothesis was that the partitioning of clients into condensates could respond to macromolecular crowding, either due to changes in the condensate per se, or due to changes in interactions between the clients and scaffolds (Nakashima et al., 2019). In support of this model, there was a significant positive monotonic correlation between GFP-MAPK3-SIM concentration in condensates and ribosome concentration ($\rho_{GFP-MAPK3} = 0.826$, $p_{GFP-MAPK3} = 0.008 < 0.01$; Figure 5F), and a corresponding correlation between GFP-MAPK3-SIM concentration and fraction hyperphosphorylation ($\rho_{GFP-MAPK3} = 0.711$, $p_{GFP-MAPK3} = 0.028 < 0.05$; Figure 5G). There was also a slight, but not significant positive correlation between mCherry-ELK1-SIM concentration and ribosome concentration ($\rho_{mCherry-ELK1} = 0.347$, $p_{Cherry-ELK1} = 0.198 > 0.05$; Figure S8E) or hyperphosphorylation ($\rho_{mCherry-ELK1} = 0.615$, $p_{Cherry-ELK1} = 0.056 > 0.05$; Figure S8F). Together, these results support the hypothesis that macromolecular crowding tunes GFP-MAPK3-SIM kinase concentration in condensates, leading to modulation of hyperphosphorylation of ELK1-SIM.

We considered compression of condensates as a second mechanism that might couple macromolecular crowding to hyperphosphorylation. We quantified the area of condensates in the same cells before and after 2 h treatment with DMSO (solvent control) or rapamycin (Figures 5H and S8G). Macromolecular crowding impacted both the degree of phase separation of $SUMO_7$-SIM_6 and the area of condensates. The most striking effect was that condensate area was substantially reduced when macromolecular crowding was increased. Increased macromolecular crowding is predicted to increase phase separation and thus increase condensate area. The fact that condensate area is decreased upon osmotic compression suggests that increased macromolecular crowding actually compresses condensates. This hypothesis predicts that condensate area should be negatively correlated with macromolecular crowding. Indeed, we see a significant negative correlation ($\rho_{area} = -0.707$, $p_{area} = 0.03 < 0.05$; Figure 5I). Together, these results support the hypothesis that macromolecular crowding leads to condensate compression, which could increase the density of client-binding sites and therefore drive more efficient hyperphosphorylation.

Phosphorylation of the Alzheimer's disease protein Tau is accelerated in condensates

Aggregation of the microtubule-associated protein, Tau, is tightly linked to the development of Alzheimer's and other neurodegenerative diseases termed tauopathies (Kovacs, 2017; Soria Lopez et al., 2019). The pathological hallmark of tauopathies are neurofibrillary tangles of hyper-phosphorylated Tau (Ihara et al., 1986). Phosphorylation destabilizes the interaction of Tau with microtubules causing mislocalization of Tau from axons to the somatodendritic compartment in neurons (Zempel and Mandelkow, 2015). It has been suggested that the concentration of Tau into liquid-like condensates could promote its conversion into fibrillar structures and thus be a critical step in Tau-induced neurotoxicity (Ambadipudi et al., 2017; Wegmann et al., 2018; Zhang et al., 2017). Multiple kinases have been reported to phosphorylate Tau (Wesseling et al., 2020), including the CDK2/Cyclin A1 complex (CDK2/CycA1) (Lee et al., 2017). However, little is known about the ability of kinases to phosphorylate Tau inside condensates and whether Tau condensation might promote Tau phosphorylation. Based on our results from synthetic

Figure 5. Synthetic condensed-phase signaling responds to changes in macromolecular crowding

(A) Representative micrographs of cells with 40 nm GEMs.

(B) Projections of GEM trajectories. Scale bars, 5 μm.

(C) Median effective diffusion coefficients D_{eff} of GEMs (left) and estimated ribosome concentrations (right) of each condition. Error bars are standard error of mean (SEM).

(D) ELK1 hyperphosphorylation levels of each strain are normalized to the mean value in DMSO; bar graphs show mean ± standard deviation (SD) (n = 3).

(E) ELK1 hyperphosphorylation shows a significant positive correlation with ribosome concentrations. Vertical error bars, SD; horizontal error bars, SEM.

(F) GFP-MAPK3-SIM intensity in condensates of each strain are normalized to the mean value of DMSO condition. There is significant positive correlation between GFP-MAPK3-SIM intensity in condensates and ribosome concentration. Vertical error bars, SD; horizontal error bars, SEM.

(G) Significant positive Spearman's rank correlation between ELK1 hyperphosphorylation and GFP-MAPK3-SIM intensity in condensates. Both vertical and horizontal error bars are SD.

(H) Fold change of $SUMO_7$-SIM_6 condensate area was measured for the same droplet before and after each treatment, and then the values were normalized to the mean value of DMSO condition of each strain. Left: mean value ± SD of normalized area fold change; each point represents a single droplet (n > 30).

(I) Significant negative Spearman's rank correlation between droplet area fold change and ribosome concentration. Vertical error bars are SD; horizontal error bars are SEM. All statistical comparisons are performed using pairwise Tukey-Kramer test: *p < 0.05, **p < 0.01, ***p < 0.001, N.S., not significant.

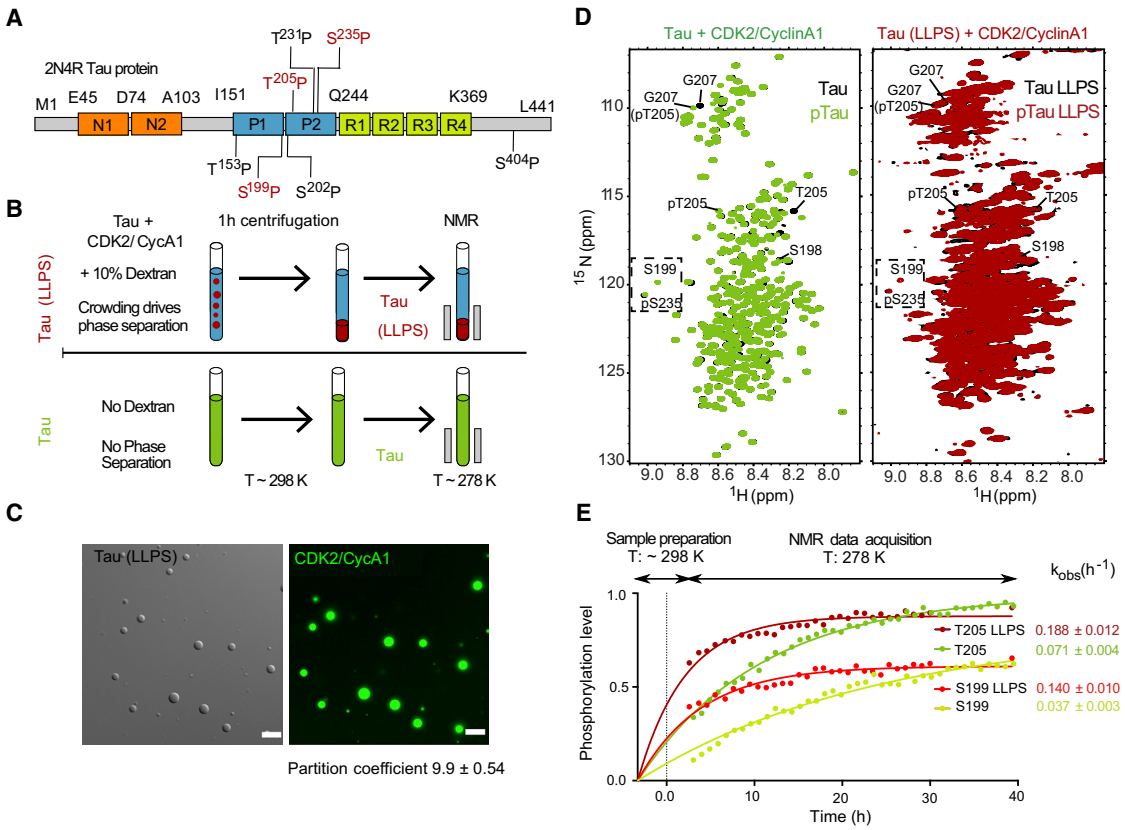

Figure 6. Phosphorylation of the Alzheimer's disease protein Tau is accelerated in condensates

(A) Domain organization of 2N4R Tau protein. Phosphorylation sites targeted by CDK2/CyclinA1 are indicated. Phosphorylated residues analyzed are displayed in red.

(B) Schematic of sample preparation. Phase separation only occurs in samples with dextran crowding agent.

(C) Fluorescence microscopy demonstrating recruitment of CDK2/CyclinA1-Alexa 488 into Tau droplets. Phase separation of Tau (40 μM) was promoted with 10% dextran. Tau and CDK2/CyclinA1-Alexa 488 were mixed using the identical molar ratio as used for the NMR experiments. The partition coefficient of CDK2/CycA1-Alexa 488 inside the tau droplets was 9.9 ± 0.54 based on fluorescence intensity analysis. Scale bars, 10 μm.

(D) Two-dimensional ^{1}H-^{15}N NMR spectroscopy. ^{1}H-^{15}N correlation spectra of Tau immediately after centrifugation are displayed in black (left panel: dispersed phase; right panel: Tau condensate). The last recorded spectrum (after ~40 h) is displayed in green (left panel, dispersed phase) or red (right panel, tau condensate). Cross-peaks of phosphorylated S235 and S199 are boxed and labeled as pS235 and pS199.

(E) Phosphorylation kinetics of S199 and T205 inside Tau condensates (red: S199; magenta: T205) and in the dispersed phase (light green: S199; green: T205). Note that the fit is extrapolated to a negative time value as a consequence of the temperature difference between sample preparation (T: 298 K) and NMR data acquisition (T: 278 K) and the phosphorylation that occurs during the centrifugation period.

condensates, we hypothesized that Tau phosphorylation might be accelerated in the condensed phase.

We used high-resolution NMR spectroscopy to compare Tau phosphorylation rates in the dispersed and condensed phases. We prepared ^{15}N-labeled 4R Tau (Figure 6A) without or with the molecular crowding agent dextran (Figure 6B). In our buffer conditions, which include approximately physiological levels of magnesium and ATP (5.6 mM $MgCl_2$, 5.6 mM ATP), phase separation only occurred in the sample with 10% dextran (Ukmar-Godec et al., 2019). CDK2/CycA1 was then added to both samples. CDK2/CycA1 phosphorylates Tau *in vitro* at phosphoepitopes associated with Alzheimer's disease (Kovacs, 2017; Savastano et al., 2021; Soria Lopez et al., 2019). We labeled CDK2/CycA1 with Alexa 488 and found strong enrichment in the condensed phase of the dextran-containing sample (partition coefficient 9.9 ± 0.54, Figure 6C). Prior to NMR measurement both samples were centrifuged for 1 h to sediment the Tau condensate in the dextran-containing sample at the bottom of the NMR tube (Figure 6B). The identical protocol in the absence of dextran created a sample without condensate allowing us to evaluate the influence of Tau condensation on Tau phosphorylation.

We recorded two-dimensional ^{1}H–^{15}N correlation spectra to quantify phosphorylation of specific Tau residues in real time (Figure 6D). Without dextran, the NMR cross-peaks displayed line shapes previously reported for Tau in the dilute phase (Figure 6D, left) (Mukrasch et al., 2009). Comparison of the first spectrum recorded after the one 1 h centrifugation period (black spectrum Figure 6D, left) with previously reported NMR spectra of unmodified Tau revealed a phosphorylation-specific cross peak for the serine residue S235 (labeled as pS235). Tau was

thus already mostly phosphorylated at S235 during sample preparation; therefore, we did not further analyze S235. In contrast, we were able to analyze phosphorylation kinetics at S199 and T205 (see green spectrum in Figure 6D, left). Cdk2/CycA1 thus rapidly phosphorylates Tau at S235, followed by phosphorylation at T205 and S199. Notably, the NMR experiments were performed at 278K (4.85°C) to improve spectral quality (due to decreased solvent exchange at low temperature) and to slow down the kinetics of phosphorylation. The changes of NMR signal position and intensity of all nonoverlapping residues indicated that CDK2/CycA1-phosphorylation only induces small, mostly local changes near the phosphorylation sites to the ensemble of Tau conformations (Figures S9A and S9B), that this lower temperature did not disrupt condensation, and that condensates did not age detectably during the experiment (Figures S9A and B). Continuous repetition of the NMR experiments over a time period of 40 h allowed the site-specific quantification of Tau phosphorylation.

Two-dimensional ^{1}H–^{15}N correlation spectra were also obtained for the sample containing the Tau condensate (right panel of Figure 6D). In agreement with previous NMR studies of condensates of intrinsically disordered proteins (e.g., Burke et al., 2015), the NMR signals were broadened due to the altered physicochemical environment (Abyzov et al., 2022). Nevertheless, we still observed the phosphorylation-specific cross peak of S235 in the spectrum recorded immediately after the 1 h centrifugation period (marked as pS235 in the black spectrum in Figure 6D, right). Thus, both in the dispersed and condensed phase, S235, which is part of the AT180 epitope, is most rapidly phosphorylated by CDK2/CycA1.

Next, we quantified the rate of phosphorylation of S199 and T205 from 40 h of repetitive ^{1}H–^{15}N correlation spectra measurements (Figure 6E). All four kinetic curves (S199 and T205 in the dispersed and condensed states) were simultaneously fit to a mono-exponential function. The fit includes a fixed phosphorylation level of 0.0 at a "negative" time point, which accounts for the 1 h of sample preparation time before the first ^{1}H–^{15}N correlation spectrum could be collected. Kinetic traces (Figure 6E) clearly showed that rates of phosphorylation of both sites were increased in the condensed phase (~3.8-fold at S199 and ~2.6-fold at T205). Thus, phosphorylation of S199 and T205, part of the Alzheimer's-disease-characteristic AT8 epitope, is accelerated in Tau condensates.

DISCUSSION

Condensates facilitate phosphoregulatory network rewiring

We found that new, dynamic kinase-substrate connections can be generated more easily within condensates than in solution, including at non-consensus phospho-acceptor motifs. It will be interesting to investigate whether the activity and substrate specificity of endogenous kinases is altered in natural condensates. The consensus sequences that are often used to predict kinase substrates may be less important in the context of condensed-phase signaling, and a larger number of possible phosphorylation sites may need to be investigated. For example, it has been shown that the crucial regulatory sites of some kinase substrates are actually at non-canonical sites; for example, degradation of the yeast cell cycle regulator Sic1 is triggered by multi-site phosphorylation including non-consensus Cdk1 sites (Kõivomägi et al., 2011; Nash et al., 2001). By extension, kinase-substrate interactions within condensates could lead to unexpected modes of phosphoregulation.

A further prediction of the ease with which we generated dynamic phosphorylation within condensates is that recruitment to condensates may facilitate the evolution of new links in phosphoregulatory networks. Phosphorylation can occur in condensates even in the absence of any obvious docking or consensus sites. It is possible that these initial phosphorylation events could provide a starting point from which useful regulation could evolve.

When mutations lead to new recruitment of kinases or substrates into condensates, more promiscuous phosphorylation could lead to gain or loss of function. For example, useful new links in phosphoregulatory networks could increase fitness, or toxic, off-target phosphorylation events, could decrease fitness. Intuitively, it seems that loss of fitness would be very likely, but in fact, we previously demonstrated that expansion of kinase specificity can be surprisingly well tolerated (Howard et al, 2014). On the other hand, our results in this study show that phosphorylation events associated with Alzheimer's disease are accelerated within Tau condensates.

Beyond mass action: Condensate flexibility and high densities of client-binding sites are important for efficient condensed-phase signaling

Recently, a number of studies have reported acceleration of biochemical activities in condensates (Huang et al., 2019; Peeples and Rosen, 2021; Poudyal et al., 2019). A recent study (Peeples and Rosen, 2021) found that reactions were accelerated by mass action. In addition, they found that certain scaffolds decreased the effective K_M of the reaction, suggesting that molecular organization was important for strong activity enhancement. Our results suggest that a flexible scaffold molecule and a large excess of client-binding sites are the most important determinants of hyperphosphorylation. We speculate that dense local clusters of binding sites organize clients within local reaction crucibles that enable processive multi-site phosphorylation.

Synthetic condensed-phase signaling can respond to biophysical changes

Recently, we found that macromolecular crowding can strongly affect biomolecular condensation (Delarue et al., 2018). Several recent examples of endogenous condensates have been reported to respond to macromolecular crowding (Cai et al., 2019). This leads to the hypothesis that there is an axis of control spanning from the global biophysical state of the cell, to mesoscale phase separation, and finally to molecular-scale biochemical reactions. We found that the degree of hyperphosphorylation in condensates responded to changes in macromolecular crowding. The ability of condensed-phase chemical reactions to respond to macromolecular crowding presents exciting new possibilities for both synthetic biology and the elucidation of new mechanisms of biological regulation and homeostasis. For example, the mechanisms that sense mechanical compression

remain poorly understood (Delarue et al., 2018), but mechanical compression leads to increases in macromolecular crowding (Alric et al., 2022); we have now demonstrated that the macromolecular crowding can modulate phosphorylation rates within condensates.

Condensed-phase phosphorylation could contribute to disease

Finally, we investigated whether naturally occurring condensates could modulate phosphorylation kinetics. Our synthetic condensates greatly increased the hyperphosphorylation of proteins. We therefore sought endogenous proteins that are associated with both condensates and hyperphosphorylation. The microtubule-associated protein Tau was a strong candidate: neurofibrillary tangles (aggregates) of hyper-phosphorylated Tau are a pathological hallmark of Alzheimer's disease (Ihara et al., 1986). Furthermore, it has been suggested that the concentration of Tau into liquid-like condensates could be an initial step in the conversion to neurofibrillary tangles (Ambadipudi et al., 2017; Wegmann et al., 2018; Zhang et al., 2017). We found phosphorylation of the Alzheimer's disease-associated AT8 epitope was accelerated 3-fold within the condensed phase. Notably, molecular crowding was required to see these effects in our reconstituted *in vitro* system. This result relates our insights from synthetic biology to possible new mechanisms for neurodegenerative disease.

Limitations of the study

In our *in vitro* experiments, we initially tried to pre-form condensates and then start reactions by addition of ATP. However, it was difficult to mix the reactions properly without disrupting the condensates. Therefore, to get reproducible results, we simultaneously formed droplets and started the kinase reaction. This approach conflates droplet formation kinetics with the kinase reaction kinetics, but condensation was similar between all conditions, allowing meaningful comparisons.

We found that p53, RPS6, and non-consensus Ser in ELK1 could all be phosphorylated by MAPK3 within synthetic condensates. The sequences surrounding the phosphorylation sites are all distinct. We currently do not understand if there are rules or patterns for kinase specificity in condensates or whether kinases like MAPK3 phosphorylate any exposed serine or threonine. However, in Figure S4H, we are able to mostly abrogate slowly migrating species in the western blot by mutating four of 100 possible phosphor-acceptor residues (77 serines, 23 threoninies) in the sequence, suggesting that phosphorylation of the min383 substrate in the condensed phase is not completely promiscuous. In future work, it will be interesting to undertake phosphoproteomics studies to get a sense of the degree to which kinase specificity is expanded.

We attempted fluorescence recovery after photobleaching (FRAP) and photoconversion experiments to quantify diffusion of clients within synthetic condensates. However, the small size of the condensates and rapid diffusion dynamics made it very difficult for us to get reliable results.

We would have liked to gain information about non-canonical phosphorylation events within Tau condensates, but the peak broadening in the condensed phase limited our ability to quantify phosphorylation of additional sites.

Compared with our synthetic systems, we have limited understanding of the mechanisms of reaction acceleration in Tau condensates, and whether mass action is sufficient to explain the effect.

Differences in *in vivo* hyperphosphorylation *in vivo* were on the order of 100-fold, whereas *in vitro* effects were smaller (2-fold to 3-fold). We speculate that systems-level effects, such as competition with phosphatases, magnify differences *in vivo*.

STAR★METHODS

Detailed methods are provided in the online version of this paper and include the following:

- KEY RESOURCES TABLE
- RESOURCE AVAILABILITY
  - Lead contact
  - Materials availability
  - Data and code availability
- EXPERIMENTAL MODEL AND SUBJECT DETAILS
  - Escherichia coli strains
  - Yeast strains
- METHOD DETAILS
  - Yeast transformation
  - Plasmid construction
  - Protein purification
  - *In vitro* kinase assays
  - MAPK3-GFP total partition calculation
  - Western blots
  - Cell perturbations
  - Phosphatase treatment of yeast lysates
  - Imaging and quantification of fluorescence intensity inside condensates and condensate size
  - HILO imaging of GEMs
  - Calculation of effective diffusion constant
  - Relative ribosome concentration calculation
  - NMR Methods
- CDK2/CyclinA1-ALEXA 488 LABELLING
- QUANTIFICATION AND STATISTICAL ANALYSIS

SUPPLEMENTAL INFORMATION

Supplemental information can be found online at https://doi.org/10.1016/j.molcel.2022.08.016.

ACKNOWLEDGMENTS

We thank Michael Rosen, Allyson Rice, and members of the HHMI Summer Institute at the Marine Biology Institute in Woods Hole for discussions that initiated this project. We thank Jef Boeke, David Engelberg, Meta Heidenreich, and Emmanuel D. Levy for sharing yeast strains and plasmids, and Greg Brittingham for help with imaging and analysis. We thank Lance Denes and Srinjoy Sil for critical reading of the manuscript. We thank the rest of the Holt lab for helpful discussions. We thank Maria-Sol Cima-Omori for preparation of ^{15}N-labeled Tau. C.F.P. acknowledges the Deutsche Akademischer Austauschdienst (DAAD) for the Research Grants Doctoral program in Germany, 2019/20 (personal ref. no. 91726791) and M.Z. was supported by the European Research Council (ERC) under the EU Horizon 2020 research and innovation program (grant agreement no. 787679). L.J.H. was funded by NIH R01 GM132447 and R37 CA240765, a donation to the American Cancer Society from the Cornelia T. Bailey Foundation, the Pershing Square Sohn Cancer

Research Award, the Chan Zuckerberg Initiative, the NIH Director's Transformative Research Award TR01 NS127186, and the Air Force Office of Scientific Research (AFoSR) Multidisciplinary University Research Initiative (MURI) competition (grant FA9550-21-1-3503 0091).

AUTHOR CONTRIBUTIONS

D.S. and T.S. undertook all experiments and analysis except NMR, supervised by L.J.H. C.F.P. undertook NMR experiments with analysis help from AIdO, supervised by M.Z. All authors contributed to writing and editing the manuscript.

DECLARATION OF INTERESTS

The authors declare no competing interests.

Received: December 8, 2021
Revised: May 18, 2022
Accepted: August 12, 2022
Published: September 14, 2022

REFERENCES

Abyzov, A., Blackledge, M., and Zweckstetter, M. (2022). Conformational dynamics of intrinsically disordered proteins regulate biomolecular condensate chemistry. Chem. Rev. *122*, 6719–6748.

Agmon, N., Mitchell, L.A., Cai, Y., Ikushima, S., Chuang, J., Zheng, A., Choi, W.J., Martin, J.A., Caravelli, K., Stracquadanio, G., and Boeke, J.D. (2015). Yeast golden gate (yGG) for the efficient assembly of *S. cerevisiae* transcription units. ACS Synth. Biol. *4*, 853–859.

Alberti, S., and Hyman, A.A. (2021). Biomolecular condensates at the nexus of cellular stress, protein aggregation disease and ageing. Nat. Rev. Mol. Cell Biol. *22*, 196–213.

Alexander, J., Lim, D., Joughin, B.A., Hegemann, B., Hutchins, J.R., Ehrenberger, T., Ivins, F., Sessa, F., Hudecz, O., Nigg, E.A., et al. (2011). Spatial exclusivity combined with positive and negative selection of phosphorylation motifs is the basis for context-dependent mitotic signaling. Sci. Signal. *4*, ra42.

Alric, B., Formosa-Dague, C., Dague, E., Holt, L.J., and Delarue, M. (2022). Macromolecular crowding limits growth under pressure. Nat. Phys. *18*, 411–416.

Ambadipudi, S., Biernat, J., Riedel, D., Mandelkow, E., and Zweckstetter, M. (2017). Liquid-liquid phase separation of the microtubule-binding repeats of the Alzheimer-related protein Tau. Nat. Commun. *8*, 275.

Amberg, D.C., Burke, D.J., and Strathern, J.N. (2006). High-efficiency transformation of yeast. CSH Protoc *2006*. pdb.prot4145.

Bähler, J., Wu, J.Q., Longtine, M.S., Shah, N.G., McKenzie, A., 3rd, Steever, A.B., Wach, A., Philippsen, P., and Pringle, J.R. (1998). Heterologous modules for efficient and versatile PCR-based gene targeting in *Schizosaccharomyces pombe*. Yeast *14*, 943–951.

Banani, S.F., Lee, H.O., Hyman, A.A., and Rosen, M.K. (2017). Biomolecular condensates: organizers of cellular biochemistry. Nat. Rev. Mol. Cell Biol. *18*, 285–298.

Banani, S.F., Rice, A.M., Peeples, W.B., Lin, Y., Jain, S., Parker, R., and Rosen, M.K. (2016). Compositional control of phase-separated cellular bodies. Cell *166*, 651–663.

Beauclair, G., Bridier-Nahmias, A., Zagury, J.F., Saïb, A., and Zamborlini, A. (2015). JASSA: a comprehensive tool for prediction of SUMOylation sites and SIMs. Bioinformatics *31*, 3483–3491.

Borchers, H.W., and Borchers, M.H.W. (2021). Package 'pracma'. (CRAN).

Bracha, D., Walls, M.T., Wei, M.T., Zhu, L., Kurian, M., Avalos, J.L., Toettcher, J.E., and Brangwynne, C.P. (2019). Mapping local and global liquid phase behavior in living cells using photo-oligomerizable seeds. Cell *176*, 407.

Burke, K.A., Janke, A.M., Rhine, C.L., and Fawzi, N.L. (2015). Residue-by-residue view of in vitro FUS granules that bind the C-terminal domain of RNA polymerase II. Mol. Cell *60*, 231–241.

Cai, D., Feliciano, D., Dong, P., Flores, E., Gruebele, M., Porat-Shliom, N., Sukenik, S., Liu, Z., and Lippincott-Schwartz, J. (2019). Phase separation of YAP reorganizes genome topology for long-term YAP target gene expression. Nat. Cell Biol. *21*, 1578–1589.

Cicenas, J., Zalyte, E., Bairoch, A., and Gaudet, P. (2018). Kinases and cancer. Cancers (Basel) *10*, 63.

Cruzalegui, F.H., Cano, E., and Treisman, R. (1999). ERK activation induces phosphorylation of Elk-1 at multiple S/T-P motifs to high stoichiometry. Oncogene *18*, 7948–7957.

Delaglio, F., Grzesiek, S., Vuister, G.W., Zhu, G., Pfeifer, J., and Bax, A. (1995). NMRPipe: a multidimensional spectral processing system based on UNIX pipes. J. Biomol. NMR *6*, 277–293.

Delarue, M., Brittingham, G.P., Pfeffer, S., Surovtsev, I.V., Pinglay, S., Kennedy, K.J., Schaffer, M., Gutierrez, J.I., Sang, D., Poterewicz, G., et al. (2018). mTORC1 controls phase separation and the biophysical properties of the cytoplasm by tuning crowding. Cell *174*, 338–349.e20.

Doolittle, A.K. (1951). Studies in Newtonian flow. II. The dependence of the viscosity of liquids on free-space. J. Appl. Phys. *22*, 1471–1475.

Elion, E.A. (2000). Pheromone response, mating and cell biology. Curr. Opin. Microbiol. *3*, 573–581.

Ellis, R.J., and Minton, A.P. (2003). Join the crowd. Nature *425*, 27–28.

Enserink, J.M., and Kolodner, R.D. (2010). An overview of Cdk1-controlled targets and processes. Cell Div *5*, 11.

Evans, E.L., Saxton, J., Shelton, S.J., Begitt, A., Holliday, N.D., Hipskind, R.A., and Shaw, P.E. (2011). Dimer formation and conformational flexibility ensure cytoplasmic stability and nuclear accumulation of Elk-1. Nucleic Acids Res *39*, 6390–6402.

Faustova, I., Bulatovic, L., Matiyevskaya, F., Valk, E., Örd, M., and Loog, M. (2021). A new linear cyclin docking motif that mediates exclusively S-phase CDK-specific signaling. EMBO J *40*, e105839.

Gibson, D.G., Young, L., Chuang, R.Y., Venter, J.C., Hutchison, C.A., 3rd, and Smith, H.O. (2009). Enzymatic assembly of DNA molecules up to several hundred kilobases. Nat. Methods *6*, 343–345.

Hastings, R.L., and Boeynaems, S. (2021). Designer condensates: a toolkit for the biomolecular architect. J. Mol. Biol. *433*, 166837.

Heidenreich, M., Georgeson, J.M., Locatelli, E., Rovigatti, L., Nandi, S.K., Steinberg, A., Nadav, Y., Shimoni, E., Safran, S.A., Doye, J.P.K., and Levy, E.D. (2020). Designer protein assemblies with tunable phase diagrams in living cells. Nat. Chem. Biol. *16*, 939–945.

Hohmann, S. (2002). Osmotic stress signaling and osmoadaptation in yeasts. Microbiol. Mol. Biol. Rev. *66*, 300–372.

Howard, C.J., Hanson-Smith, V., Kennedy, K.J., Miller, C.J., Lou, H.J., Johnson, A.D., Turk, B.E., and Holt, L.J. (2014). Ancestral resurrection reveals evolutionary mechanisms of kinase plasticity. eLife *3*, e04126.

Huang, W.Y.C., Alvarez, S., Kondo, Y., Lee, Y.K., Chung, J.K., Lam, H.Y.M., Biswas, K.H., Kuriyan, J., and Groves, J.T. (2019). A molecular assembly phase transition and kinetic proofreading modulate Ras activation by SOS. Science *363*, 1098–1103.

Ihara, Y., Nukina, N., Miura, R., and Ogawara, M. (1986). Phosphorylated Tau protein is integrated into paired helical filaments in Alzheimer's disease. J. Biochem. *99*, 1807–1810.

Kõivomägi, M., Valk, E., Venta, R., Iofik, A., Lepiku, M., Balog, E.R., Rubin, S.M., Morgan, D.O., and Loog, M. (2011). Cascades of multisite phosphorylation control Sic1 destruction at the onset of S phase. Nature *480*, 128–131.

Kovacs, G.G. (2017). Tauopathies. Handb. Clin. Neurol. *145*, 355–368.

Lee, D.S.W., Wingreen, N.S., and Brangwynne, C.P. (2021). Chromatin mechanics dictates subdiffusion and coarsening dynamics of embedded condensates. Nat. Phys. *17*, 531–538.

Lee, K.H., Lee, S.J., Lee, H.J., Choi, G.E., Jung, Y.H., Kim, D.I., Gabr, A.A., Ryu, J.M., and Han, H.J. (2017). Amyloid beta1-42 (Abeta1-42) induces the CDK2-mediated phosphorylation of Tau through the activation of the

mTORC1 signaling pathway while promoting neuronal cell death. Front. Mol. Neurosci. *10*, 229.

Lee, W., Tonelli, M., and Markley, J.L. (2015). NMRFAM-SPARKY: enhanced software for biomolecular NMR spectroscopy. Bioinformatics *31*, 1325–1327.

Levin-Salomon, V., Kogan, K., Ahn, N.G., Livnah, O., and Engelberg, D. (2008). Isolation of intrinsically active (MEK-independent) variants of the ERK family of mitogen-activated protein (MAP) kinases. J. Biol. Chem. *283*, 34500–34510.

Li, P., Banjade, S., Cheng, H.C., Kim, S., Chen, B., Guo, L., Llaguno, M., Hollingsworth, J.V., King, D.S., Banani, S.F., et al. (2012). Phase transitions in the assembly of multivalent signalling proteins. Nature *483*, 336–340.

Li, W., Hamill, S.J., Hemmings, A.M., Moore, G.R., James, R., and Kleanthous, C. (1998). Dual recognition and the role of specificity-determining residues in colicin E9 DNase-immunity protein interactions. Biochemistry *37*, 11771–11779.

Luby-Phelps, K. (1999). Cytoarchitecture and physical properties of cytoplasm: volume, viscosity, diffusion, intracellular surface area. In International review of cytology, H. Walter, D.E. Brooks, and P.A. Srere, eds. (Academic Press), pp. 189–221.

Malumbres, M. (2014). Cyclin-dependent kinases. Genome Biol *15*, 122.

Miller, C.J., and Turk, B.E. (2018). Homing in: mechanisms of substrate targeting by protein kinases. Trends Biochem. Sci. *43*, 380–394.

Miyamoto, T., DeRose, R., Suarez, A., Ueno, T., Chen, M., Sun, T.P., Wolfgang, M.J., Mukherjee, C., Meyers, D.J., and Inoue, T. (2012). Rapid and orthogonal logic gating with a gibberellin-induced dimerization system. Nat. Chem. Biol. *8*, 465–470.

Mok, J., Kim, P.M., Lam, H.Y., Piccirillo, S., Zhou, X., Jeschke, G.R., Sheridan, D.L., Parker, S.A., Desai, V., Jwa, M., et al. (2010). Deciphering protein kinase specificity through large-scale analysis of yeast phosphorylation site motifs. Sci. Signal. *3*, ra12.

Mukrasch, M.D., Bibow, S., Korukottu, J., Jeganathan, S., Biernat, J., Griesinger, C., Mandelkow, E., and Zweckstetter, M. (2009). Structural polymorphism of 441-residue Tau at single residue resolution. PLoS Biol *7*, e34.

Mylona, A., Theillet, F.X., Foster, C., Cheng, T.M., Miralles, F., Bates, P.A., Selenko, P., and Treisman, R. (2016). Opposing effects of Elk-1 multisite phosphorylation shape its response to ERK activation. Science *354*, 233–237.

Nakashima, K.K., Vibhute, M.A., and Spruijt, E. (2019). Biomolecular chemistry in liquid phase separated compartments. Front. Mol. Biosci. *6*, 21.

Namanja, A.T., Li, Y.J., Su, Y., Wong, S., Lu, J., Colson, L.T., Wu, C., Li, S.S., and Chen, Y. (2012). Insights into high affinity small ubiquitin-like modifier (SUMO) recognition by SUMO-interacting motifs (SIMs) revealed by a combination of NMR and peptide array analysis. J. Biol. Chem. *287*, 3231–3240.

Nash, P., Tang, X., Orlicky, S., Chen, Q., Gertler, F.B., Mendenhall, M.D., Sicheri, F., Pawson, T., and Tyers, M. (2001). Multisite phosphorylation of a CDK inhibitor sets a threshold for the onset of DNA replication. Nature *414*, 514–521.

Örd, M., and Loog, M. (2019). How the cell cycle clock ticks. Mol. Biol. Cell *30*, 169–172.

Örd, M., Möll, K., Agerova, A., Kivi, R., Faustova, I., Venta, R., Valk, E., and Loog, M. (2019). Multisite phosphorylation code of CDK. Nat. Struct. Mol. Biol. *26*, 649–658.

O'Rourke, S.M., and Herskowitz, I. (1998). The Hog1 MAPK prevents cross talk between the HOG and pheromone response MAPK pathways in *Saccharomyces cerevisiae*. Genes Dev *12*, 2874–2886.

Peeples, W., and Rosen, M.K. (2021). Mechanistic dissection of increased enzymatic rate in a phase-separated compartment. Nat. Chem. Biol. *17*, 693–702.

Poudyal, R.R., Guth-Metzler, R.M., Veenis, A.J., Frankel, E.A., Keating, C.D., and Bevilacqua, P.C. (2019). Template-directed RNA polymerization and enhanced ribozyme catalysis inside membraneless compartments formed by coacervates. Nat. Commun. *10*, 490.

Rawat, P., Boehning, M., Hummel, B., Aprile-Garcia, F., Pandit, A.S., Eisenhardt, N., Khavaran, A., Niskanen, E., Vos, S.M., Palvimo, J.J., et al. (2021). Stress-induced nuclear condensation of NELF drives transcriptional downregulation. Mol. Cell *81*, 1013–102.6.e11.

Reményi, A., Good, M.C., and Lim, W.A. (2006). Docking interactions in protein kinase and phosphatase networks. Curr. Opin. Struct. Biol. *16*, 676–685.

Savastano, A., Flores, D., Kadavath, H., Biernat, J., Mandelkow, E., and Zweckstetter, M. (2021). Disease-associated Tau phosphorylation hinders tubulin assembly within Tau condensates. Angew. Chem. Int. Ed. Engl. *60*, 726–730.

Schindelin, J., Arganda-Carreras, I., Frise, E., Kaynig, V., Longair, M., Pietzsch, T., Preibisch, S., Rueden, C., Saalfeld, S., Schmid, B., et al. (2012). Fiji: an open-source platform for biological-image analysis. Nat. Methods *9*, 676–682.

Schindelin, J., Rueden, C.T., Hiner, M.C., and Eliceiri, K.W. (2015). The ImageJ ecosystem: an open platform for biomedical image analysis. Mol. Reprod. Dev. *82*, 518–529.

Schulman, B.A., Lindstrom, D.L., and Harlow, E. (1998). Substrate recruitment to cyclin-dependent kinase 2 by a multipurpose docking site on cyclin A. Proc. Natl. Acad. Sci. USA *95*, 10453–10458.

Shin, Y., Berry, J., Pannucci, N., Haataja, M.P., Toettcher, J.E., and Brangwynne, C.P. (2017). Spatiotemporal control of intracellular phase transitions using light-activated optoDroplets. Cell *168*, 159–171.e14.

Shin, Y., and Brangwynne, C.P. (2017). Liquid phase condensation in cell physiology and disease. Science *357*, eaaf4382.

Shivanandan, A., Radenovic, A., and Sbalzarini, I.F. (2013). MosaicIA: an ImageJ/Fiji plugin for spatial pattern and interaction analysis. BMC Bioinformatics *14*, 349.

Sikorski, R.S., and Hieter, P. (1989). A system of shuttle vectors and yeast host strains designed for efficient manipulation of DNA in *Saccharomyces cerevisiae*. Genetics *122*, 19–27.

Soria Lopez, J.A., González, H.M., and Léger, G.C. (2019). Alzheimer's disease. Handb. Clin. Neurol. *167*, 231–255.

Stegmeier, F., and Amon, A. (2004). Closing mitosis: the functions of the Cdc14 phosphatase and its regulation. Annu. Rev. Genet. *38*, 203–232.

Tang, X., Orlicky, S., Mittag, T., Csizmok, V., Pawson, T., Forman-Kay, J.D., Sicheri, F., and Tyers, M. (2012). Composite low affinity interactions dictate recognition of the cyclin-dependent kinase inhibitor Sic1 by the SCFCdc4 ubiquitin ligase. Proc. Natl. Acad. Sci. USA *109*, 3287–3292.

Tinevez, J.Y., Perry, N., Schindelin, J., Hoopes, G.M., Reynolds, G.D., Laplantine, E., Bednarek, S.Y., Shorte, S.L., and Eliceiri, K.W. (2017). TrackMate: an open and extensible platform for single-particle tracking. Methods *115*, 80–90.

Ukmar-Godec, T., Hutten, S., Grieshop, M.P., Rezaei-Ghaleh, N., Cima-Omori, M.S., Biernat, J., Mandelkow, E., Söding, J., Dormann, D., and Zweckstetter, M. (2019). Lysine/RNA-interactions drive and regulate biomolecular condensation. Nat. Commun. *10*, 2909. https://doi.org/10.1038/s41467-019-10792-y.

Verdecia, M.A., Bowman, M.E., Lu, K.P., Hunter, T., and Noel, J.P. (2000). Structural basis for phosphoserine-proline recognition by group IV WW domains. Nat. Struct. Biol. *7*, 639–643.

Visintin, R., Craig, K., Hwang, E.S., Prinz, S., Tyers, M., and Amon, A. (1998). The phosphatase Cdc14 triggers mitotic exit by reversal of Cdk-dependent phosphorylation. Mol. Cell *2*, 709–718.

Wegmann, S., Eftekharzadeh, B., Tepper, K., Zoltowska, K.M., Bennett, R.E., Dujardin, S., Laskowski, P.R., MacKenzie, D., Kamath, T., Commins, C., et al. (2018). Tau protein liquid-liquid phase separation can initiate Tau aggregation. EMBO J *37*.

Wesseling, H., Mair, W., Kumar, M., Schlaffner, C.N., Tang, S., Beerepoot, P., Fatou, B., Guise, A.J., Cheng, L., Takeda, S., et al. (2020). Tau PTM profiles identify patient heterogeneity and stages of Alzheimer's disease. Cell *183*, 1699–1713.e13.

Wippich, F., Bodenmiller, B., Trajkovska, M.G., Wanka, S., Aebersold, R., and Pelkmans, L. (2013). Dual specificity kinase DYRK3 couples stress granule condensation/dissolution to mTORC1 signaling. Cell *152*, 791–805.

Zempel, H., and Mandelkow, E.M. (2015). Tau missorting and spastin-induced microtubule disruption in neurodegeneration: Alzheimer disease and hereditary spastic paraplegia. Mol. Neurodegener. *10*, 68.

Zhang, H., Cao, X., Tang, M., Zhong, G., Si, Y., Li, H., Zhu, F., Liao, Q., Li, L., Zhao, J., et al. (2021a). A subcellular map of the human kinome. eLife *10*, e64943.

Zhang, X., Lin, Y., Eschmann, N.A., Zhou, H., Rauch, J.N., Hernandez, I., Guzman, E., Kosik, K.S., and Han, S. (2017). RNA stores Tau reversibly in complex coacervates. PLoS Biol *15*, e2002183.

Zhang, Y., Lee, D.S.W., Meir, Y., Brangwynne, C.P., and Wingreen, N.S. (2021b). Mechanical frustration of phase separation in the cell nucleus by chromatin. Phys. Rev. Lett. *126*, 258102.

STAR★METHODS

KEY RESOURCES TABLE

REAGENT or RESOURCE	SOURCE	IDENTIFIER
Antibodies		
anti-Elk1	9182	Cell signaling; RRID: AB_2277936
anti-p-Elk1(Ser383)	9181	Cell signaling; RRID: AB_2099016
anti-p-Erk1(T202/Y204)	4377	Cell signaling; RRID: AB_331775
anti-HA	12CA5	Roche; RRID: AB_2920713
anti-p-P53(S37)	9289	Cell signaling; RRID: AB_2210689
anti-p-P53(S9)	9288	Cell signaling; RRID: AB_331470
anti-Rps6(S235/236)	2211	Cell signaling; RRID: AB_331679
Bacterial and virus strains		
Rosetta (DE3) Competent Cells - Novagen	Millipore Sigma	Cat# 70954-3
E.coli XL-1 Blue	Agilent	Cat# 200249
Chemicals, peptides, and recombinant proteins		
Gibson Assembly Master mix	NEB	Cat# E2611S
[γ-32P]ATP	Perkin Elmer	Cat# BLU002250UC
Ni-NTA Beads	Qiagen	Cat# 30210
PD-10 desalting column	GE	Cat# 17085101
Rapamycin	Tocris Bioscience	Cat# 1292
Sorbitol	Sigma-Aldrich	Cat# S1876
Lambda Protein Phosphatase	NEB	Cat# P0753S
GA3-AM	Tocris Bioscience	Cat. No. 5407
Experimental models: Organisms/strains		
S.cerevisiae: W303 MATa leu2-3, 112 trip1-1 can1-100 ura3-1 ade2-1 ade2-1 his3-11-,15	DOM0090	David Morgan Lab
W303 + HIS3::PRpl18-mCherry-Elk1WT-1SIM	LH-DJ001	Holt lab
W303 + HIS3::PRpl18-mCherry-Elk1WT-1SIM, LEU2::PPAB1-GFP-ERK1R84S-1SIM	LH-DJ002	Holt lab
W303 + HIS3::PRpl18-mCherry-Elk1WT-1SIM, URA3::PTDH3-SUMO2	LH-DJ003	Holt lab
W303 + HIS3::PRpl18-mCherry-Elk1WT-1SIM, URA3::PTDH3-SUMO10-SIM6	LH-DJ004	Holt lab
W303 + HIS3::PRpl18-mCherry-Elk1WT-1SIM, LEU2::PPAB1-GFP-ERK1R84S-1SIM, URA3::PTDH3-SUMO2	LH-DJ005	Holt lab
W303 + HIS3::PRpl18-mCherry-Elk1WT-1SIM, LEU2::PPAB1-GFP-ERK1R84S-1SIM, URA3::PTDH3-SUMO10-SIM6	LH-DJ006	Holt lab
W303 + HIS3::PRNR2-mCherry-Elk1DM-1SIM	LH-DJ007	Holt lab
W303 + HIS3::PRNR2-mCherry-Elk1DM-1SIM, LEU2::PPAB1-GFP-ERK1R84S-1SIM	LH-DJ008	Holt lab

(*Continued on next page*)

Continued

REAGENT or RESOURCE	SOURCE	IDENTIFIER
W303 + HIS3::PRNR2-mCherry-Elk1DM-1SIM, URA3::PTDH3-SUMO2	LH-DJ009	Holt lab
W303 + HIS3::PRNR2-mCherry-Elk1DM-1SIM, URA3::PTDH3-SUMO10-SIM6	LH-DJ010	Holt lab
W303 + HIS3::PRNR2-mCherry-Elk1DM-1SIM, LEU2::PPAB1-GFP-ERK1R84S-1SIM, URA3::PTDH3-SUMO2	LH-DJ011	Holt lab
W303 + HIS3::PRNR2-mCherry-Elk1DM-1SIM, LEU2::PPAB1-GFP-ERK1R84S-1SIM, URA3::PTDH3-SUMO10-SIM6	LH-DJ012	Holt lab
W303 + HIS3::PRpl18-mCherry-Elk1WT11APMU-1SIM	LH-DJ013	Holt lab
W303 + HIS3::PRpl18-mCherry-Elk1WT11APMU-1SIM, LEU2::PPAB1-GFP-ERK1R84S-1SIM, URA3::PTDH3-SUMO10-SIM6	LH-DJ014	Holt lab
W303 + HIS3::PRpl18-mCherry-Elk1WT-1SIM, LEU2::PPAB1-GFP-ERK1R84S-1SIM, URA3::PTDH3-SUMO10-SIM6	LH-DJ015	Holt lab
W303 + HIS3::PRNR2-mCherry-Elk1DM-1SIM,FUS3-GFP-2SIM::KANMX, URA3::PTDH3-SUMO2	LH-DJ016	Holt lab
W303 + HIS3::PRNR2-mCherry-Elk1DM-1SIM,FUS3-GFP-2SIM::KANMX, URA3::PTDH3-SUMO10-SIM6	LH-DJ017	Holt lab
W303 + HIS3::PRNR2-mCherry-Elk1DM-1SIM,CDC28-GFP-1SIM::KANMX	LH-DJ018	Holt lab
W303 + HIS3::PRNR2-mCherry-Elk1DM-1SIM,CDC28-GFP-1SIM::KANMX, URA3::PTDH3-SUMO2	LH-DJ019	Holt lab
W303 + HIS3::PRNR2-mCherry-Elk1DM-1SIM,CDC28-GFP-1SIM::KANMX, URA3::PTDH3-SUMO10-SIM6	LH-DJ020	Holt lab
W303 + HIS3::PRpl18-mCherry-Elk1WT-1SIM,TRP::PRNR2-2XNES-GFP-2XWW, LEU2::PPAB1-GFP-ERK1R84S-1SIM, URA3::PTDH3-SUMO10-SIM6	LH-DJ021	Holt lab
W303 + HIS3::PRpl18-mCherry-Elk1WT-1SIM,TRP::PRNR2-2XNES-GFP-2XWW, LEU2::PPAB1-GFP-ERK1K71R-1SIM, URA3::PTDH3-SUMO10-SIM6	LH-DJ022	Holt lab
W303 + HIS3::PTDH3-mCherry-2xElk1DM-3SIM,TRP::PRPL18-1xNLS-GFP-2XWW, LEU2::PTDH3-2xNLS-BFP, URA3::PTDH3-SUMO10-SIM6	LH-DJ023	Holt lab
W303 + HIS3::PTDH3-mCherry-2xElk1DM-3SIM,TRP::PRPL18-1xNLS-GFP-2XWW, LEU2::PTDH3-2xNLS-BFP, CDC28-mCherry-1SIM::KANMX, URA3::PTDH3-SUMO10-SIM6	LH-DJ024	Holt lab
W303 + HIS3::PRPL18-mCherry-EPCT383-5SIM	LH-DJ025	Holt lab

(*Continued on next page*)

Continued

REAGENT or RESOURCE	SOURCE	IDENTIFIER
W303 + HIS3::PRPL18-mCherry-EPCT383-5SIM, LEU2::PPAB1-GFP-ERK1R84S-5SIM	LH-DJ026	Holt lab
W303 + HIS3::PRPL18-mCherry-EPCT383-5SIM, URA3::PTDH3-SUMO10-SIM6	LH-DJ027	Holt lab
W303 + HIS3::PRPL18-mCherry-EPCT383-5SIM, LEU2::PPAB1-GFP-ERK1R84S-5SIM, URA3::PTDH3-SUMO2	LH-DJ028	Holt lab
W303 + HIS3::PRPL18-mCherry-EPCT383-5SIM, LEU2::PPAB1-GFP-ERK1R84S-5SIM, URA3::PTDH3-SUMO2	LH-DJ029	Holt lab
W303 + LEU2::PPAB1-GFP-ERK1R84S-5SIM, URA3::SUMO10-SIM6 HIS3::PRPL18-mCherry-EPCT383-5SIM,	LH-DJ030	Holt lab
W303 + LEU2::PPAB1-GFP-ERK1R84S-5SIM, URA3::SUMO10-SIM6, HIS3::PRPL18-mCherry-EPCT383-5SIM truncation	LH-DJ031	Holt lab
W303 + LEU2::PPAB1-GFP-ERK1R84S-5SIM, URA3::SUMO10-SIM6, HIS3::PRPL18-mCherry-EPCT383-5SIM S394Del	LH-DJ032	Holt lab
W303 + LEU2::PPAB1-GFP-ERK1R84S-5SIM, URA3::PSUMO10-SIM6, HIS3::PRPL18-mCherry-EPCT383-5SIM S375A	LH-DJ033	Holt lab
W303 + LEU2::PPAB1-GFP-ERK1R84S-5SIM, URA3::SUMO10-SIM6, HIS3::PRPL18-mCherry-EPCT383-5SIM 4SDel	LH-DJ034	Holt lab
W303 + LEU2::PPAB1-GFP-ERK1R84S-5SIM, HIS3::PRPL18-mCherry-EPCT383-5SIM	LH-DJ035	Holt lab
W303 + LEU2::PPAB1-GFP-ERK1R84S-5SIM, HIS3::PRPL18-mCherry-EPCT383-5SIM truncation	LH-DJ036	Holt lab
W303 + HIS3::PRpl18-mCherry-PR-3SIM	LH-DJ037	Holt lab
W303 + HIS3::PRpl18-mCherry-PR-3SIM,CDC28-GFP-1SIM::KANMX	LH-DJ038	Holt lab
W303 + HIS3::PRpl18-mCherry-PR-3SIM,URA3::PTDH3-SUMO10-SIM6	LH-DJ039	Holt lab
W303 + HIS3::PRpl18-mCherry-PR-3SIM,CDC28-GFP-1SIM::KANMX,URA3::PTDH3-SUMO10-SIM6	LH-DJ040	Holt lab
W303 + HIS3::PRpl18-mCherry-PR-3SIM,CDC28-GFP-1SIM::KANMX,URA3::PTDH3-SUMO2	LH-DJ041	Holt lab
W303 + HIS3::PRNR2-mCherry-Elk1DMI9P-1SIM, LEU2::PPAB1-GFP-ERK1R84S-1SIM, URA3::PTDH3-SUMO10-SIM6	LH-DJ042	Holt lab
W303 + HIS3::PRNR2-mCherry-Elk1DM-1SIM, LEU2::PPAB1-GFP-ERK1R84S-1SIM, URA3::PTDH3-SUMO10-SIM6	LH-DJ043	Holt lab
W303 + HIS3::PRPL18-mCherry-Elk1DM-1SIMI9P, LEU2::PPAB1-GFP-ERK1R84S-1SIM, URA3::PTDH3-SUMO10-SIM6	LH-DJ044	Holt lab
W303 + HIS3::PRNR2-mCherry-Elk1DM-2SIM, LEU2::PPAB1-GFP-ERK1R84S-2SIM, URA3::PTDH3-SUMO10-SIM6	LH-DJ045	Holt lab
W303 + HIS3::PRPL18-mCherry-Elk1DM-1SIM, LEU2::PRPL18-GFP-ERK1R84S-1SIM, URA3::PTDH3-SUMO10-SIM6	LH-DJ046	Holt lab
W303 + HIS3::PRNR2-mCherry-Elk1DM-1SIM, LEU2::PPAB1-GFP-ERK1R84S-1SIM, URA3::PTDH3-SUMO7-SIM6	LH-DJ047	Holt lab
W303 + HIS3::PRPL18mCherry-Elk1DM-1SIM, LEU2::PRPL18-GFP-ERK1R84S-1SIM	LH-DJ048	Holt lab

(*Continued on next page*)

Continued

REAGENT or RESOURCE	SOURCE	IDENTIFIER
W303 + HIS3::PRPL18mCherry-Elk1DM-1SIM, LEU2::PRPL18-GFP-ERK1R84S-1SIM, URA3::PTDH3-SUMO7-SIM6	LH-DJ049	Holt lab
W303 + HIS3::PRpl18-mCherry-Elk1WT-1SIM, LEU2::PRPL18-GFP-ERK1R84S-1SIM, URA3::PTDH3-Dimer-1SUMO	LH-DJ050	Holt lab
W303 + HIS3::PRpl18-mCherry-Elk1DM-1SIM, LEU2::PRPL18-GFP-ERK1R84S-1SIM, URA3::PTDH3-Dimer-1SUMO, TRP::PTDH3-Hexamer	LH-DJ051	Holt lab
W303 + HIS3::PRpl18-mCherry-Elk1DM-1SIM, LEU2::PRPL18-GFP-ERK1R84S-1SIM, URA3::PTDH3-Dimer-2SUMO, TRP::PTDH3-Hexamer	LH-DJ052	Holt lab
W303 + HIS3::PRpl18-mCherry-Elk1DM-1SIM, LEU2::PRPL18-GFP-ERK1R84S-1SIM, URA3::PTDH3-Dimer-3SUMO, TRP::PTDH3-Hexamer	LH-DJ053	Holt lab
W303 + HIS3::PRpl18-mCherry-Elk1DM-1SIM, LEU2::PRPL18-GFP-ERK1R84S-1SIM, URA3::PTDH3-Dimer-weak08-1SUMO, TRP::PTDH3-Hexamer	LH-DJ054	Holt lab
W303 + HIS3::PRNR2-mCherry-Elk1DM-1SIM, LEU2::PPAB1-GFP-ERK1R84S-1SIM, URA3::PTDH3-SUMO7-SIM6, hog1Δ::KANMX	LH-DJ055	Holt lab
W303 + HIS3::PRNR2-mCherry-Elk1DM-1SIM, LEU2::PPAB1-GFP-ERK1R84S-1SIM, URA3::PTDH3-Dimer-weak08-1SUMO, *TRP*::PTDH3-Hexamer, *hog1Δ*::KANMX	LH-DJ056	Holt lab
W303 + HIS3::PRNR2-mCherry-Elk1DM-1SIM, LEU2::PPAB1-GFP-ERK1R84S-1SIM, URA3::PTDH3-Dimer-weak08-1SUMO, hog1Δ::KANMX	LH-DJ057	Holt lab
W303 + HIS3::PRNR2-mCherry-Elk1DM-1SIM, LEU2::PPAB1-GFP-ERK1R84S-1SIM, URA3::PTDH3-SUMO2, *hog1Δ*::KANMX	LH-DJ058	Holt lab
W303 + HIS3::PRNR2-mCherry-Elk1DM-1SIM, LEU2::PPAB1-GFP-ERK1R84S-1SIM, URA3::PTDH3-SUMO10, *TRP*::PTDH3-Hexamer-1SIM, *hog1Δ*::KANMX	LH-DJ059	Holt lab
W303 + HIS3::PRNR2-mCherry-Elk1DM-1SIM, LEU2::PPAB1-GFP-ERK1R84S-1SIM, URA3::PTDH3-SUMO10-SIM6, hog1Δ::KANMX	LH-DJ060	Holt lab
W303 + HIS3::PRpl18-mCherry-Elk1DM-1SIM, LEU2::PRPL18-GFP-ERK1R84S-1SIM, URA3::PTDH3-SUMO7-SIM6, *hog1Δ*::KANMX	LH-DJ061	Holt lab
W303 + HIS3::PRNR2-mCherry-Elk1DM-1SIM, LEU2::PPAB1-GFP-ERK1R84S-1SIM, URA3::PTDH3-Dimer-weak08-1SUMO, *TRP*::PTDH3-Hexamer, *hog1Δ*::KANMX	LH-DJ062	Holt lab
W303 + HIS3::PRNR2-mCherry-Elk1DM-1SIM, LEU2::PPAB1-GFP-ERK1R84S-1SIM, URA3::PTDH3-SUMO7-SIM6, hog1Δ::KANMX, sfp1Δ::KANMX	LH-DJ063	Holt lab
W303 + HIS3::PRNR2-mCherry-Elk1DM-1SIM, LEU2::PPAB1-GFP-ERK1R84S-1SIM, URA3::PTDH3-SUMO7-SIM6, *hog1Δ*::KANMX, *fus3Δ*::NATMX	LH-DJ064	Holt lab
BY4741 + LEU2::PINO4-PFV-GS-Sapphire	LH4258	Holt lab
BY4741 + sfp1Δ::HPHNT1 + LEU2::PINO4-PFV-GS-Sapphire	LH4259	Holt lab
Recombinant DNA		
pAV103-PRpl18-mCherry-Elk1WT-1SIM	pLH-DJ001	Holt lab
pAV103-PRNR2-mCherry-Elk1DM-1SIM	pLH-DJ002	Holt lab
pAV103-PRpl18-mCherry-Elk1DM-1SIM	pLH-DJ003	Holt lab
pAV103-PRpl18-mCherry-Elk1WT11APMU-1SIM	pLH-DJ004	Holt lab

(*Continued on next page*)

Continued

REAGENT or RESOURCE	SOURCE	IDENTIFIER
pAV103-PRNR2-mCherry-Elk1DMI9P-1SIM	pLH-DJ005	Holt lab
pAV103-PRPL18-mCherry-Elk1DMI9P-1SIM	pLH-DJ006	Holt lab
pAV103-PRPL18-mCherry-EPCT383-5SIM	pLH-DJ007	Holt lab
pAV103-PRPL18-mCherry-EPCT383Trncation-5SIM	pLH-DJ008	Holt lab
pAV103-PRPL18-mCherry-EPCT383S394Del-5SIM	pLH-DJ009	Holt lab
pAV103-PRPL18-mCherry-EPCT383S375A-5SIM	pLH-DJ010	Holt lab
pAV103-PRPL18-mCherry-EPCT3834SDEL-5SIM	pLH-DJ011	Holt lab
pAV103-PRpl18-mCherry-PR-3SIM	pLH-DJ012	Holt lab
pAV103-PTDH3-mCherry-2xElk1DM-3SIM	pLH-DJ013	Holt lab
pAV103-PRNR2-mCherry-Elk1DM-1SIMI9P	pLH-DJ014	Holt lab
pAV103-PRPL18-mCherry-Elk1DM-1SIMI9P	pLH-DJ015	Holt lab
pAV103-PRNR2-mCherry-Elk1DM-2SIM	pLH-DJ016	Holt lab
pAV105-PPAB1-GFP-Erk1R84S-1SIM	pLH-DJ017	Holt lab
pAV105-PRPL18-GFP-Erk1R84S-1SIM	pLH-DJ018	Holt lab
pAV105-PPAB1-mCherry-Erk1R84S-3SIM	pLH-DJ019	Holt lab
pAV105-PPAB1-mCherry-Erk1K71R-3SIM	pLH-DJ020	Holt lab
pAV105-PPAB1-GFP-Erk1R84S-5SIM	pLH-DJ021	Holt lab
pAV105-PPAB1-GFP-Erk1R84S-2SIM	pLH-DJ022	Holt lab
pAV105-PPAB1-GFP-Erk1R84S-3SIM	pLH-DJ023	Holt lab
pAV105-PTDH3-2xNLS-BFP	pLH-DJ024	Holt lab
pRS306-PTDH3-SUMO2	pLH-DJ025	Holt lab
pRS306-PTDH3-SUMO10	pLH-DJ026	Holt lab
pRS306-PTDH3-SUMO10-6SIM	pLH-DJ027	Holt lab
pRS306-PTDH3-Dimer-1SUMO	pLH-DJ028	Holt lab
pRS306-PTDH3-Dimer-2SUMO	pLH-DJ029	Holt lab
pRS306-PTDH3-Dimer-3SUMO	pLH-DJ030	Holt lab
pRS306-PTDH3-Dimer-weak08-1SUMO	pLH-DJ031	Holt lab
pRS306-PTDH3-SUMO7-6SIM	pLH-DJ032	Holt lab
pRS3304-PRNR2-2XNES-GFP-2XWW	pLH-DJ033	Holt lab
pRS3304-RPL18-1xNLS-GFP-2XWW	pLH-DJ034	Holt lab
pRS3304-PTDH3-HEXAMER	pLH-DJ035	Holt lab
pRS3304-PTDH3-HEXAMER-1SIM	pLH-DJ036	Holt lab
pET28b-SUMO10	pLH-DJ037	Holt lab
pET28b-FKBP12-6SIM	pLH-DJ038	Holt lab
pET28b-FRB-mCherry-Erk1	pLH-DJ039	Holt lab
pET28b-FRB-GFP-Elk1	pLH-DJ040	Holt lab
pFA6a-CDK-GFP-1SIM	pLH-DJ041	Holt lab
pFA6a-FUS3-GFP-2SIM	pLH-DJ042	Holt lab
Software and algorithms		
FIJI (FIJI is just image J)	Schindelin et al., 2012	http://www.nature.com/nmeth/journal/v9/n7/full/nmeth.2019.html
Image J2	Schindelin et al., 2015	http://onlinelibrary.wiley.com/https://doi.org/10.1002/mrd.22489/full
MOSAIC for ImageJ	Shivanandan et al., 2013	https://bmcbioinformatics.biomedcentral.com/articles/10.1186/1471-2105-14-349
MATLAB 2019a	MathWorks, Inc.	https://www.mathworks.com/products/matlab.html
Nikon Elements	Nikon Instruments, Inc.	https://www.nikoninstruments.com/Products/Software

(*Continued on next page*)

Continued

REAGENT or RESOURCE	SOURCE	IDENTIFIER
pcrma package	Borchers and Borchers, 2021	https://cran.r-project.org/web/packages/pracma/index.html
Scripts for droplet properties analysis and GEM & Ribosome concentration analysis	This article	https://doi.org/10.5281/zenodo.6979049

RESOURCE AVAILABILITY

Lead contact

Further information and requests for resources aCnd reagents should be directed to and will be fulfilled by the lead contact, Liam J. Holt (liam.holt@nyulangone.org).

Materials availability

All materials will be made available on request.

Data and code availability

- All data reported in this paper will be shared by the lead contact upon request.
- All code is available at: https://doi.org/10.5281/zenodo.6979049.
- Any additional information required to reanalyze the data reported in this work paper is available from the Lead Contact upon request.

EXPERIMENTAL MODEL AND SUBJECT DETAILS

Escherichia coli strains

XL-1 blue competent bacterial strains were grown in lysogeny broth (LB) containing antibiotic selection in a shaking incubator at 220 rpm, 37°C.

Rosetta2 DE3 competent cells were grown in LB containing antibiotic selection in a shaking incubator at 220 rpm for 18 h at 16°C. Recombinant protein expression was induced by addition of 100 μM IPTG.

Yeast strains

Plasmids were transformed into W303 strain and grown in a rotating drum incubator in synthetic dropout (SD) media –Leu, -His, -Trp, or –Ura, respectively at 30°C.

METHOD DETAILS

Yeast transformation

Yeast strains were created by transforming with a LiAc based approach according to Cold Spring Harbor Protocols (Amberg et al., 2006). All strains were constructed in the W303 strain background (*MATa leu2-3, 112 trip1-1 can1-100 ura3-1 ade2-1 ade2-1 his3-11-,15*). A list of strains built is provided in Table S1. To tag Cdk1 and Fus3 with GFP-SIM, pFA6a-CDK-GFP-SIM or pFA6a-FUS3-GFP-2xSIM, the plasmid was cut within the coding sequences of Cdk1 or Fus3, and the linearized plasmid was then transformed, leading to recombination into the endogenous locus. As the plasmids do not contain a promoter, this leads to a tagged allele, and inactivation of the endogenous allele.

Plasmid construction

The open reading frames encoding $SUMO_{10}$-SIM_6 condensates, GFP-MAPK3-1SIM and mCherry-ELK1-1SIM were chemically synthesized (Qinglan, China). The $SUMO_{10}$-SIM_6 condensate expression plasmid in yeast was constructed by fusion 5' end of the ORF with the strong promoter from *TDH3* by Gibson assembly (Gibson et al., 2009) into the pRS306 vector (Sikorski and Hieter, 1989). Plasmids for kinase expression in yeast were constructed with either a weak (from the *PAB1* gene), or medium promoter (from the *RPL18* gene) by Gibson assembly into the pAV105 vector (Agmon et al., 2015). Substrate expression plasmids were similarly constructed with either yeast weak (from the *RNR2* gene), or medium (from the *RPL18* gene) promoters in the pAV103 vector (Agmon et al., 2015). To express the rigid synthetic condensate components in yeast, the dimer and hexamer components were amplified by PCR and assembled into pRS306 vector or pRS304 vector (Sikorski and Hieter, 1989) by Gibson assembly. The WW reporter was generated by fusion of GFP to a tandem repeat of the WW domain from Peptidyl-prolyl cis-trans isomerase NIMA-interacting 1, *Homo sapiens*. This protein was expressed from the promoter of the *RPL18* gene and assembled into the pRS304 vector (Sikorski and Hieter, 1989). To tag Cdk1 and Fus3 with GFP-SIM, Cdk1/Fus3 CDS, GFP and SIM tag were amplified and assembled into pFA6a

vector (Sikorski and Hieter, 1989) by Gibson (Bähler et al., 1998). All yeast plasmids were integrated into the host genome. pET28b vectors were used for bacterial expression. Open Reading Frames (ORFs) of the $SUMO_{10}$, FKBP12-SIM_6, FRB-mCherry-MAPK3 and FRB-GFP-ELK1 proteins were fused at the N terminus to the 6x histidine tag for purification. The ORFs and the vectors were Gibson assembled. A list of plasmids constructed is provided in Table S2.

Protein purification

Protein purification from *E. coli* cells was performed as previously described (Howard et al., 2014). Briefly, proteins were expressed in Rosetta2 DE3 competent cells by induction with 100 μM IPTG for 18 hr at 16°C. Bacterial culture were collected and centrifuged at 4000 rpm for 20 min at 4°C. The cell pellet was resuspended in cold lysis buffer (50 mM NaH2PO4, 300 mM NaCl, 10 mM imidazole pH7.6, 1 mM PMSF). After sonication, the lysate was centrifuged at 12000 rpm for 20 min at 4°C. The supernatant was mixed with magnetic Ni-NTA beads (Qiagen) and incubated for 2 hr at 4°C. The bound beads were collected and rinsed 3 × with wash buffer containing (50 mM NaH2PO4, 300 mM NaCl, 20 mM imidazole pH7.6). The bound proteins were eluted with elution buffer (50 mM NaH2PO4, 300 mM NaCl, 500 mM imidazole pH7.6). The eluted proteins were concentrated using Amicon® Ultra Centrifugal Filters (Millipore Sigma). The concentrated proteins were dialyzed into SUMO-SIM protein buffer (150 mM KCl, 20 mM HEPES pH 7, 1 mM MgCl2, 1 mM EGTA, 1 mM DTT) with 10% glycerol using PD10 columns (GE Healthcare), followed by further concentration using an Amicon Ultra 30K device (Millipore) at 4C, and finally flash frozen in aliquots with liquid nitrogen and stored at -80°C.

In vitro kinase assays

For phosphorylation in condensates, the components for kinase reaction and condensate formation were divided into two halves, each with a 10 μl volume. Combination of these two mixtures initiated the kinase reaction. The first half contained 30 μM FKBP12-SIM_6, 40 nM FRB-GFP-MAPK3, 8 μM FRB-mCherry-ELK1, 50 μM Rapamycin (or same volume of DMSO), 10 mM $MgCl_2$ and 75 mM KCl. Components were equilibrated for 20 minutes. The phosphorylation was started by addition of the second half, which contained 24 μM $SUMO_{10}$, 200 μM ATP, 10 mM $MgCl_2$, 75 mM KCl and 0.1 μCi of [γ-32P]ATP. The two halves were mixed thoroughly by gentle pipetting. Reactions were carried out at room temperature for 5 minutes and terminated by addition of 10 μl 5x SDS loading buffer (10% SDS, 0.5 M DTT, 50% glycerol, 0.25% Bromophenol blue). All samples were separated on 4–12% Bis-Tris gels (ThermoFisher Scientific). The gel was dried and exposed to a phosphor screen. Phosphor screens were analyzed with a Typhoon 9500 scanner (GE) using ImageQuant software (GE).

MAPK3-GFP total partition calculation

While the reaction proceeded, the other half of the solution was transferred to a 384-well glass bottomed imaging plates and imaged using an Andor Yokogawa CSU-X confocal spinning disc on a Nikon TI Eclipse microscope. Fluorescence was recorded with a sCMOS Prime95B camera (Photometrics) with a 100x objective (pixel size: 0.11um). A stack of 50 images were acquired at 1μM intervals from the bottom of the plate upwards. A blank well with buffer was imaged to determine the camera background value. This background value was subtracted from every image. The fluorescence integrated density of 'drops' or 'solvent' in the 488 and 561 channels was calculated using a classifier mask derived from contrast adjusted imaged segmented with the trainable Weka Segmentation package on default settings. The condensates are denser than the solution and sediment near the bottom of the well. Therefore, the reaction is asymmetrically distributed along the z axis and symmetric along the x & y axes. We reasoned that it would be necessary to calculate the total protein in the solvent and condensates along the entire vertical stack to calculate the total partition of a given volume. It was calculated that given the volume of reaction added to the well, there would be an additional 2490 'slices' spaced out every 1uM on top of the 50 μM imaged. It was observed that condensates never formed in slices 48-51 as the condensates had sedimented below this point. It should also be noted that carefully controlling temperature and evaporation are required to prevent solution turbidity. Therefore, the average solvent protein concentration was determined by finding the mean integrated density per slice in this 'top of the well' equivalent from slices 48-51. Next, the condensate and solvent protein concentrations across the entire well were calculated by integrating along the slices using the 'trapz' function from the pcrma package (Borchers and Borchers, 2021). To calculate total MAPK3-GFP partition , the total protein in condensates was divided by the total concentration in solution across the entire y dimension. The scripts used for partition coefficient calculation are provided in supplementary files as QC1 and QC2.

Western blots

Cell cultures were grown to OD 0.6–0.8. Cells were collected and treated with 1M LiAc for 5 min on ice. After centrifugation cell pellets were treated with 0.4M NaOH for 5 min. Then cells were centrifuged again, and were suspended in SDS-PAGE sample buffer and boiled for 5min. Supernatant samples were separated on 10% SDS-PAGE gels and transferred to Immobilon-FL PVDF membrane (Millipore). Membranes were probed with primary antibodies, including anti-p-ELK1-S383, anti-ELK1, anti-p-MAPK3, anti-ERK2, anti-Tubulin, anti-HA, anti-p-P53-S37, anti-p-P53-S9, anti-p-RPS6-S235/236 and anti-p-Sata3-Y705 (key resources table in STAR Methods), and corresponding secondary IRDye 800CW antibodies (LI-COR Biosciences). Band intensities were quantified with Image Studio™ analysis software (LI-COR Biosciences).

For hyperphosphorylation (Hypershift/Tubulin) quantification, the intensity signal of hypershifted phosphorylated band (detected by anti-p-ELK1-S383, which is indicated by the red arrowheads in the western blot gel figure) was normalized to the intensity signal of tubulin band (detected by anti-Tubulin).

Cell perturbations

For α factor experiments, cells were grown to log phase (OD 0.2 - 0.8) and then treated with 2 μM α factor for up to 1 h, then collected by centrifugation for 3min at 3000g and lysed for western blot.

For sorbitol treatments, log phase cells were collected by centrifugation for 3min at 3000g. Cells were then suspended in media with or without 1 M sorbitol, grown for 1h, and then collected and lysed as above.

For rapamycin treatment, log phase cells were incubated with DMSO (solvent control) or 1 μM rapamycin for 2h. Then cells were collected as above for western blot.

For treatment with rapamycin combined with sorbitol, cells were first incubated with 1 μM rapamycin for 1 h or 1 μM DMSO (solvent control), then collected by centrifugation for 3min at 3000g. Cells were next resuspended in media with 1 μM rapamycin or 1 μM DMSO, with or without 1 M sorbitol for an additional 1 h. Then cells were collected and lyses as above.

Phosphatase treatment of yeast lysates

Yeast cell were collected when the culture OD reach 0.8. Cells were pretreated with 0.4M NaOH for 2 min on ice. After centrifugation, cell pellets were suspended in lysis buffer with protease inhibitor tablet (Pierce) and lysed by bead beating. Then samples were centrifuged at 800g for 2 minutes. The supernatants were incubated with lambda protein phosphatase (NEB) according to the manufacturer's protocol. For treatment with phosphatase inhibitor, NaF (final 50 mM), β-glycerol phosphate (final 50 mM), and Na3VO4 (final 1 mM) were added. The lysates were incubated at 30°C for 30 minutes and terminated by addition of 5x SDS loading buffer followed by boiling for 5 minutes.

Imaging and quantification of fluorescence intensity inside condensates and condensate size

Cells were imaged using TIRF Nikon TI Eclipse microscope in epifluorescence mode, and fluorescence was recorded with an sCMOS camera (Zyla, Andor) with a 100x objective. GFP and mCherry channel images were generated by average projection of 13 z-slices with 0.4 μm spacing (4.8 μm total). Condensate properties within cells were characterized using the TrackMate ImageJ plugin (Schindelin et al., 2012; Schindelin et al., 2015; Tinevez et al., 2017). Due to relatively higher intensity and higher contrast in GFP fluorescent signals, condensates in GFP channel were first detected using LoG (Laplacian of Gaussian filter) detector with one micron 'Estimated blob diameter' and a fixed 'Threshold' across all experimental conditions. For each individual image with both GFP and mCherry channels, the number of detected condensates within the GFP channel was then recorded and was used as a criterion for choosing the 'Threshold' parameter for condensate detection in the mCherry channel. The 'Estimated blob diameter' parameter for mCherry condensate detection still maintained as one. Using this method, the majority of condensates detected in both channels overlapped with each other. Particle detection results from TrackMate were saved as *xml* files. We then extracted and compiled particle properties in both channels, especially condensate mean pixel intensity, using home-written MATLAB code. In addition, we also extracted the background mean pixel intensity by randomly selecting 20 circles in each image from areas away from cellular condensates. Thus, the final condensate mean pixel intensity were calculated by subtracting the background mean pixel intensity from condensate mean pixel intensity identified above.

For calculation of condensate area and client concentration changes, log-phase cells were immobilized in 384-well imaging plates coated with concanavalin A (ConA). GFP and mCherry channel images were generated by average projection of 13 z-slices with 0.4 μm spacing (4.8 μm total). For experiments with sorbitol treatment only, immobilized cells were imaged, then media was carefully removed and replaced with media containing 1M sorbitol, and the same cells were imaged again after 1h. For experiments under various conditions, such as rapamycin treatment, cells were immobilized, imaged and then media was carefully changed, and cells were imaged again after 2h with 1 μM rapamycin. For treatment with rapamycin and sorbitol, cells were imaged, then were treated sequentially with 1μM rapamycin for 1h, then old medium was removed and incubated with fresh SCM with 1μM rapamycin and 1M sorbitol for a further 1h, and cells were imaged again. Condensates were identified manually based on their GFP signal, and the area of the same condensate before and after treatment was calculated by measurement in Image J (Schindelin et al., 2012; Schindelin et al., 2015).

HILO imaging of GEMs

GEM particles in *S. cerevisiae* yeast cells were imaged using Highly inclined thin illumination (HILO) TIRF Nikon TI Eclipse microscope in partial TIRF mode under 100% power of 488nm excitation laser. The emitted fluorescent signals were transmitted through a 100x objective (100x Phase, Nikon, oil NA = 1.4, part number = MRD31901) and recorded with a sCMOS camera (Zyla, Andor, part number = ZYLA-4.2p-CL10). The GFP filter set (ET-EGFP (FITC/Cy2), Chroma, part number = 49002) was embedded within the light path, which includes an excitation filter (Excitation wavelength/ Bandwidth (FWHM) = 470/40 nm), a dichroic mirror (long pass beamsplitter, reflecting < 495 nm and transmitting > 495 nm wavelength) and an emission filter (Emission wavelength/ Bandwidth (FWHM) = 525/50 nm). Each GEM movie was recorded at a single focal plane with 10 ms frame rate with no delay (100 Hz) for a total of 4 s (400 frames

total), using Nikon NIS-Elements Advanced Research software. Trajectories of GEM particles from each GEM movie were subsequently analyzed using Mosaic plugin in ImageJ/FIJI (Schindelin et al., 2012; Schindelin et al., 2015; Shivanandan et al., 2013).

Calculation of effective diffusion constant

For every 2D GEM trajectory, we calculated the time-averaged mean-square displacement (MSD) at different time intervals:

$$<\Delta r^2(\tau)>_T = <[x(t+\tau) - x(t)]^2 + [y(t+\tau) - y(t)]^2>_T \quad \text{(Equation 1)}$$

where '$<>_T$' represents time averaging for each trajectory of all displacements for time interval τ.

To reduce statistical error, we limited our analyses to particle trajectories with longer than 10 time points. The time-averaged MSD for each trajectory was then fitted for the first 10 time intervals:

$$MSD(\tau)_T = 4D_{eff}\tau \quad \text{(Equation 2)}$$

where D_{eff} is effective diffusion coefficient for each trajectory (units of $\mu m^2/s$).

For each experimental condition, we then used the median value of D_{eff} from all trajectories (typically thousands of trajectories from hundreds of cells) and plotted bar graphs with error bars as standard error of the mean.

Relative ribosome concentration calculation

We inferred ribosome concentration based on a model derived from the phenomenological Doolittle equation (Doolittle, 1951; Delarue et al., 2018).

$$\log\left(\frac{D}{D_0'}\right) = \zeta\frac{\varphi_0/\varphi_m}{1-\varphi_0/\varphi_m}\frac{1-c_{ribo-rela}}{1-c_{rib0-rela*}\varphi_0/\varphi_m} \quad \text{(Equation 3)}$$

where D represents the experimentally observed effective diffusion coefficient, D_0' represents the effective diffusion coefficient in control conditions, φ_0 is the volume fraction of macromolecules in control conditions, φ_m is the maximum volume fraction of macromolecules when it no longer possible to remove water from the cell, ζ is a dimensionless parameter, representing the interaction strength between the probe particle and its surrounding environment, $c_{ribo-rela}$ is the relative ribosomal concentration compared to control conditions.

When cells are exposed to an instantaneous osmotic pressure, the number of macromolecules can be approximated as unchanged. Thus, $c_{ribo-rela}$ would become the inverse of the normalized cell volume compared to control condition, i.e. $1/\tilde{v}$, where $\tilde{v}$ is the normalized cell volume. By observing the effective diffusion coefficient of GEMs under different osmotic pressures, and measuring the corresponding cell volume (approximating the cell as prolate ellipsoid in brightfield images), the equation parameters: ζ, φ_0/φ_m were obtained by fitting equation (4).

$$\log\left(\frac{D}{D_0'}\right) = \zeta\frac{\varphi_0/\varphi_m}{1-\varphi_0/\varphi_m}\frac{\tilde{v}-1}{\tilde{v}-\varphi_0/\varphi_m} \quad \text{(Equation 4)}$$

NMR Methods

Sample preparation for Tau phosphorylation experiment

^{15}N-labeled Tau protein (2N4R Tau; hTau40) was expressed in *Escherichia coli* strain BL21(DE3) from a pNG2 vector (a derivative of pET-3a, Merck-Novagen, Darmstadt) in presence of an antibiotic. Cells were grown, centrifuged at low speed, washed with M9 salts (Na_2HPO_4, KH_2PO_4 and NaCl) and resuspended in minimal medium M9 supplemented with $^{15}NH_4Cl$ as the only nitrogen source and induced with 0.5 mM IPTG. Subsequently, cells were disrupted with a French pressure cell press in lysis buffer (20 mM MES pH 6.8, 1 mM EGTA, 2 mM DTT) complemented with protease inhibitor mixture, 0.2 mM $MgCl_2$, lysozyme and DNAse I. NaCl was added to a final concentration of 500 mM and boiled for 20 minutes. Denaturated proteins were removed by ultracentrifugation at 4 °C. Salt was removed by dialysis and the sample was filtered and purified by ion exchange and gel filtration chromatography. Finally, the protein was dialyzed against HEPES buffer, pH 6.8.

NMR samples were prepared by adding 1 mM TCEP, 5.6 mM $MgCl_2$, 0.1 mM PMSF, 5.6 mM ATP, 5.6% D_2O and 1 mM DSS. The reference sample volume was 180 µl and the LLPS sample, supplemented with 10% dextran T500, reached a final volume of 770 µl in order to get a good amount of the condensate phase that fills the NMR coil. The final protein concentration was 168 µM in both cases. After introducing the sample into a 3 mm Shigemi NMR tube the CDK2/CycA3 enzyme was added with a final concentration of 6.4 µg/ml. The samples were mixed followed by centrifugation at ~1500 g for one hour at room temperature. The reference sample received the same treatment in order to start the experiment in an equivalent condition.

NMR experiments and kinetics analysis

Two-dimensional ^{1}H-^{15}N heteronuclear single quantum coherence (HSQC) experiments were acquired at 278 K on a Bruker 900 MHz spectrometer equipped with a triple-resonance 5 mm cryogenic probe. Spectra were processed with NMRPipe (Delaglio et al., 1995) and analyzed using Sparky (Lee et al., 2015). Despite increased signal overlap in the condensed phase, careful analysis of the sufficiently separated cross-peaks of T205 and S198 (which is neighboring the phosphorylated S199; Figure 6C, right panel) provided

single-residue access to the phosphorylation kinetics inside the Tau condensate (Figure 6D). Peak intensities were extracted from a series of two-dimensional ^{1}H-^{15}N HSQC data sets at one-hour time intervals. After peak assignment using the previously established resonance assignment (Mukrasch et al., 2009), the peak intensities were normalized with respect to the peak intensity of the C-terminal residue (L441). The resulting values were then normalized to the reference intensity values (non-phosphorylated sample) for each phosphorylated residue and analyzed with GraphPad Prism by fitting to first-order decay kinetics. As the temperature during sample preparation was around 298 K (faster phosphorylation kinetics) and the experiment was measured at 278 K, the zero time of the analyzed 278 K kinetics is expected to be negative. This problem was solved by global fitting of the starting point t_0 for all analyzed residues according to:

$$P = A(1 - \exp(-K_{obs}(t - t_0))$$

The four phosphorylation kinetic traces, i.e. S199 in the dispersed phase, T205 in the dispersed phase, S199 in the Tau condensate and T205 in the Tau condensate, were simultaneously fitted to a single value of t_0.

CDK2/CyclinA1-ALEXA 488 LABELLING

CDK2/CyclinA1 was labeled with Alexa Fluor 488 on lysine residues employing Microscale Protein Labeling Kit (Thermo Fisher Scientific). DIC and fluorescence images were recorded using a Leica DM6000B microscope with a 63x objective (water immersion). Imaging analyses were performed using FIJI software ((Schindelin et al., 2012), NIH).

QUANTIFICATION AND STATISTICAL ANALYSIS

Statistical analyses were performed using MATLAB R2019a. Statistical differences between samples within a group were assessed using one-way analysis of variance (ANOVA) and subsequently pairwise post-hoc Tukey-Kramer test, with *: $p<0.05$, **: $p<0.01$, ***: $p<0.001$, N.S.: $p \geq 0.05$. Correlation statistics between two variables were performed using Spearman's rank correlation (ρ), which assesses monotonic relationships whether linear or not. P values were generated based on the null hypothesis of either there is no positive correlation or there is no negative correlation. All quantitative data are presented as the mean ± SEM or ± SD of biologically independent samples (n), unless stated otherwise. Statistical analysis was carried out using MATLAB R2019a software. Statistical differences between samples within a group were assessed using one-way analysis of variance (ANOVA) and subsequently pairwise post-hoc Tukey-Kramer test, *$p<0.05$, **$p<0.01$, **$p<0.001$, N.S. (not significant) $p \geq 0.05$. Spearman's rank correlation was used to assess correlation statistics between two variables.